Fermi National Accelerator Laboratory

FERMILAB-Pub-93/001

E705

The Experiment 705 Electromagnetic Shower Calorimeter

L. Antoniazzi et al.
The E705 Collaboration

Fermi National Accelerator Laboratory
P.O. Box 500, Batavia, Illinois 60510

January 1993

Submitted to *Nuclear Instruments and Methods A*

Operated by Universities Research Association Inc. under Contract No. DE-AC02-76CHO3000 with the United States Department of Energy

Disclaimer

The Experiment 705 Electromagnetic Shower Calorimeter

L. Antoniazzi[3], M. Arenton[9] , Z. Cao[8], T.Y. Chen[5], S. Conetti[4], B. Cox[9], S. Delchamps[3], L. Fortney[2], K. Guffey[7], M. Haire[4], M. He[8], P. Ioannou[1], C. M. Jenkins[3], D. J. Judd[7], C. Kourkoumelis[1], A. Manousakis-Katsikakis[1], J. Kuzminski[4], T. LeCompte[6], A. Marchionni[4], P. O. Mazur[3], C. T. Murphy[3], P. Pramantiotis[1], R. Rameika[3], L. Resvanis[1], M. Rosati[4], J. Rosen[6], C. H. Shen[8], Q. Shen[2], A. Simard[4], R. Smith[3], L. Spiegel[3], D. Stairs[4], Y. Tan[6], R. J. Tesarek[2], T. Turkington[2], L. Turnbull[4], F. Turkot[3], S. Tzamarias[6], G. Voulgaris[1], D. E. Wagoner[7], C. Wang[8], J. Weckel[2], W. Yang[3], N. Yao[5], N. Zhang[8], X. Zhang[8], G. Zioulas[4], B. Zou[2]

(1) University of Athens, Athens, Greece
(2) Duke University, Durham, NC
(3) Fermi National Accelerator Laboratory, Batavia, IL
(4) McGill University, Montreal, Quebec, Canada
(5) Nanjing University, People's Republic of China
(6) Northwestern University, Evanston, IL
(7) Prairie View A&M University, Prairie View, TX
(8) Shandong University, Shandong, People's Republic of China
(9) University of Virginia, Charlottesville, VA

Abstract

Experiment 705 at Fermi National Accelerator Laboratory has designed, built, and operated a large acceptance, highly segmented electromagnetic shower calorimeter using SF5 lead glass, SCG1-C scintillating glass, and two types of gas-based fine-grained hodoscopes. The calorimeter was used to reconstruct photons and electrons with energies ranging from a few GeV/c² to over 100 GeV/c² in 300 GeV/c pion and proton interactions on a lithium target at instantaneous interaction rates approaching several MHz. Construction details of the calorimeter are given. The readout electronics, calibration, and algorithms used to reconstruct the positions and energies of showering particles are discussed. Energy resolution, position resolution, and reconstruction efficiency are assessed using both calibration electron beams and electrons and π^0 mesons reconstructed in 300 GeV/c interactions.

1. INTRODUCTION

Fermilab Experiment 705 [1] used interactions induced by 300 GeV/c hadrons on a lithium target to accomplish two primary physics goals, both of which demanded the efficient and accurate measurement of photon energies and production angles, as well as off-line identification and rejection of photons from the decays of neutral mesons, mainly π^0 and η^0.

The reconstruction of the radiative decays of the $\chi_1(3510)$ and $\chi_2(3555)$ states of charmonium demanded excellent photon energy resolution at relatively low energies, ~2-25 GeV/c^2. The acceptance of the photon detector had to be large enough to accept a reasonable fraction of the photons from the radiative decay

$$\chi \rightarrow J/\psi(3097) + \gamma$$

The majority of photons, even in events containing a radiative χ decay, are associated with $\pi^0 \rightarrow \gamma\gamma$, and had to be eliminated off-line. Since low energy π^0's can have large opening angles, this requirement puts further demands on the geometrical acceptance of the calorimeter.

The other major goal of Experiment 705 was the measurement of direct photons, so called because they are believed to emerge directly from the scattering of hadronic constituents, and not from the decays of other particles. To measure direct photons effectively, photons with transverse momenta greater than about 3 GeV/c and a large range of laboratory polar angles had to be properly reconstructed. The implied photon energy range for Experiment 705 was $10 < E < 200$ GeV/c^2. Position resolution had to be sufficient to distinguish between high energy single photons and closely spaced pairs of photons from the decays of high energy π^0's.

The calorimeter described in this paper presented an area of ~4 x 2 m^2 at a distance of 10 meters from the experimental target. It employed over 400 scintillating and lead glass blocks for detection of most of the energy of showering particles, and two highly segmented gas tube devices for position determination of electromagnetic showers. The relatively long time scale of the run (~8 months) required a schedule of regular calibrations as well as accurate monitoring of changes in electronic gains and pedestals. To keep changes in the gains to a minimum required low radiation damage and excellent temperature stability. Finally, to collect enough events of interest,

interaction rates approaching 1 MHz were needed, and a special system of readout electronics was devised to handle high interaction rates.

2. MECHANICAL DESCRIPTION

Figure 1 is a top view of the Experiment 705 electromagnetic shower calorimeter. The beam direction is indicated by an arrow. Most of the energy of a showering electron or photon was deposited in the Main Array glass blocks. Depending upon which part of the calorimeter a particle entered, showering began in the Active Converter glass blocks (divided into front and rear portions) or the layers of the Lead Gas Calorimeter (LGC). Transverse shower positions were measured in a coarse manner by the division of energy between the blocks of the Active Converter and Main Array, and much more finely by the LGC and Gas Tube Hodoscope (GTH). The entire calorimeter was housed in a movable structure so that during calibrations each main array block could be centered in a calibration beam of electrons or positrons.

2.1 The Main Array

A beam view of the 375 cm x 195 cm Main Array is shown in Figure 2. A 30 cm x 15 cm central hole allowed beam particles which did not interact in the experimental target to pass through without depositing energy in the calorimeter. Two types of glass, SF5 lead glass and SCG1-C scintillating glass, the properties of which are shown in Table 1, were used in the Main Array. In the Main Array central region, 7.5 x 7.5 x 89 cm^3 and 15 x 15 x 89 cm^3 SCG1-C scintillating glass blocks [2, 3, 4] were used. These blocks were 20.9 radiation lengths and 2.0 nuclear absorption lengths (for pions in the energy range 30-200 GeV/c^2) deep in the beam direction. In the outer region of the Main Array, SF5 lead glass blocks 15 x 15 x 41.5 cm^3 were used. The SF5 blocks were 16.8 radiation lengths and 1.0 nuclear absorption lengths in depth. The SF5 and SCG1-C glass converted some fraction of the energy of showering particles into light, which was then collected by photomultiplier tubes mounted on the rear surface of each Main

Array block. Each Main Array block was wrapped in aluminized mylar and black tape to keep out stray light.

The light collected in lead glass is Cerenkov radiation from the electrons and positrons in an electromagnetic shower. The photomultiplier tube charge pulses due to Cerenkov light are narrow (~20 nsec), making lead glass ideal for high-rate applications. However, radiation damage can cause lead glass to darken, limiting the amount of light collected for a given deposited energy. Two kinds of light are produced in SCG1-C in response to electromagnetic showers: There is Cerenkov radiation as in lead glass, although in SCG1-C the radiator is barium oxide instead of lead oxide. There is also scintillation light from the excitation and relaxation of cerium oxide. (Cerium oxide also shifts the Cerenkov light to lower frequencies where it is more efficiently transmitted by the glass.) About 5.1 times the light for a given parent particle energy is available in SCG1-C relative to SF5 [2, 3]; this leads to an improvement in the intrinsic energy resolution for SCG1-C by reducing the photon sampling fluctuations by a factor of about $\sqrt{5}$.

In addition to its improved light yield, SCG1-C was found to be about 150 times as resistant to radiation damage as SF5 glass [4]. For this reason, the SCG1-C blocks were placed in the central region of the Main Array, where most particles produced in interactions in the experimental target enter the calorimeter.

2.2 Active Converter

Figure 3 is a beam view of the Active Converter and LGC. The East and West Active Converters were sets of 30 SCG1-C blocks with dimensions 7.5 x 7.5 x 97.5 cm^3 arranged in columns two blocks high and two blocks deep (15 cm). The West and East Active Converters covered the Main Array regions $x > 52$ cm and $x < -52$ cm respectively, where the horizontal and vertical (x and y) origin of coordinates is defined to lie along the beam axis, which passes through the center of the beam hole. The scintillating glass in the Active Converter represented 3.5 radiation lengths and 0.3 nuclear absorption lengths in the beam direction. There was a 1.3 cm thick steel pre-radiator upstream of the Active Converter. The blocks in the Active Converter were wrapped in the same way as the Main Array blocks. Between the Active Converter and the front face of the Main Array there was a 14 cm gap, occupied by the GTH.

The Active Converter (plus the pre-radiator) served three purposes: The thickness in radiation lengths was sufficient to begin the showering of most photons and electrons. In addition, the SCG1-C glass allowed the measurement of the energy of the initial part of the shower. Finally, the division of the Active Converter into 7.5 cm wide columns gave a coarse shower position measurement in the horizontal direction.

2.3 Lead Gas Calorimeter

Like the Active Converter, the Lead Glass Calorimeter or LGC [5] served as shower starter and as an energy and position measuring device. Because the small-angle region occupied by the LGC was more highly populated with showers, the LGC had to have a higher degree of spatial segmentation than the Active Converter.

The LGC was a 103 cm x 195 cm eight-layer sampling device covering the central region ($|x|<52$ cm) of the Main Array, as shown in Figure 3. A section of the LGC viewed from the top is shown in Figure 4.

Each layer of the LGC contained a row of extruded aluminum sheets forming three-sided tubes. Thirteen eight-tube extrusions (EASCO Corp., Phoenix, Arizona) were placed together to form a single panel. A 0.05 cm sheet of resistive PVC (not shown in the Figure 4) formed the fourth wall of the tubes in the panel. The tubes were nearly square in cross section, with 0.84 cm wall separation and 0.16 cm wall thickness. The tubes had center-mounted 50 micron diameter gold-plated tungsten wires held at +1.85 kV relative to the tube walls. The transverse wire pitch was 0.99cm. Signals read out from the tube wires gave horizontal shower position and energy information.

A 0.16 cm thick G-10 board and a 0.12 cm thick lead sheet were placed next to the PVC sheet of each LGC layer. The G-10 boards had 0.8 cm wide copper stripes with 1.25 cm pitch on the side facing the PVC sheet. The stripes were aligned perpendicular to the tube axes, so that induced signals on the stripes gave vertical shower position and energy information.

The tube row closest to the target was preceded by a pre-radiator consisting of 1.3 cm of steel (0.7 radiation lengths) and 0.8 cm of lead (1.4 radiation lengths). The tubes were filled with 50/50 argon-ethane bubbled through isopropyl alcohol at 5° C. An input gas manifold insured

uniform flow of gas through the tubes. The LGC was ~3.8 radiation lengths deep in the beam direction.

The aluminum extrusions defined 104 vertically aligned tubes in each LGC layer. The upper and lower halves of each tube were instrumented by independent wires. The eight wires from tubes at the same horizontal position were electronically ganged to form a single signal.

The copper stripes were divided into two groups. The division between the left and right stripe groups is shown as a bold s-shaped line in Figure 3. The stripes nearest the center of the LGC in the vertical dimension were half-length. Sets of stripes at the same vertical coordinate were electronically ganged.

The LGC had a central region filled only with argon-ethane, which matched the central hole in the Main Array.

2.4 Gas Tube Hodoscope

The Gas Tube Hodoscope or GTH [6] was designed to measure the positions of showers in the region of the calorimeter covered by the Active Converter. GTH panels 156 cm x 197 cm in area were positioned between the East and West Active Converter stacks and the Main Array, as shown in Figure 1. The East and West GTH panels each had a 10 cm overlap with the LGC. A section of the GTH is shown in Figure 5.

Each GTH panel consisted of two planes of polystyrene tubes. The tubes were rectangular with inner dimensions 0.73 cm x 1.00 cm. Tubes in the regions $x < -85$ cm and $x > 85$ cm had the dimensions formed by two standard adjacent tubes with the 0.16 cm dividing wall removed. (This region is referred to below as the double-tube region.) Each tube had a center-mounted 50 micron diameter gold-plated tungsten wire. The wire pitches for the standard and double size cells were 0.88 cm and 1.76 cm respectively. The same gas mixture as for the LGC was circulated through the tubes.

The tube planes were epoxied between three planes of 0.16 cm thick G-10 printed circuit board. The central printed circuit board had blank copper plating on both sides, and served as a ground plane for the wires in the tubes, which were held at +1.9 kV relative to ground. A conducting mixture of graphite powder and Scotch 2216 Amber structural adhesive was used to

attach the tube planes to the ground plane printed circuit board. The front and rear printed circuit boards were identical to those used for the LGC horizontal stripes. As in the LGC, tubes and stripes at the same horizontal and vertical positions were electronically ganged, and the wires and stripes gave horizontal and vertical shower position information, respectively.

2.5 Calorimeter Housing

The electromagnetic calorimeter rested on a table approximately 4 1/2 m wide and 2 m deep, as shown schematically in Figure 6. The stack of Main Array blocks, the GTH, the LGC, and the Active Converter stack all rested on the upstream part of the table. The rear of the table was reserved for access to the photomultiplier tubes, bases, and cabling.

A thermally insulated housing surrounded the calorimeter, and a blower and heat exchanger system together with the insulation kept the interior temperature from varying by more than ±0.5° F, contingent on the external environment not varying by more than ± 5° F.

The table was supported by four screw jacks. The frame supporting the screw jacks rested in a pit sunk into the cement floor of the experimental hall, so that the calorimeter and housing could be moved ±1 m vertically about the vertical level of the beam. The frame had rollers at the bottom, which allowed the entire structure to be moved back and forth ±2 m transverse to the beam direction. The horizontal and vertical motions were used during calibration, as described in Section 4.3 of this paper.

The motors which drove the horizontal and vertical motions could be operated locally with hand switches or remotely by CAMAC commands issued by a Motorola VME/10 personal computer. Encoder chains were used to register the horizontal and vertical positions of the calorimeter in 0.05 cm increments. When the table was operated locally, the horizontal and vertical encoder readouts were available on LED displays; in remote mode, the positions were available from the VME/10 computer in hexadecimal form, in centimeters, or in terms of the block number on which the beam was currently centered.

Two tilt switches independently registered table tilt about the beam and horizontal axes. Out-of-tolerance readings on either tilt switch disabled the calorimeter motion.

3. INSTRUMENTATION AND ELECTRONICS

3.1 Glass Electronics

The 15 x 15 cm^2 and 7.5 x 7.5 cm^2 blocks of the Main Array were instrumented with EMI 9791KB and RCA 6342A photomultiplier tubes respectively. The Active Converter blocks were instrumented with RCA 6342A photomultiplier tubes. An optical couplant (Dow Corning 92-3067) was used to seal the phototube windows and the rear faces of the glass blocks. Transistorized bases designed at Fermilab were used on both types of tubes to minimize sagging of the phototube gains at high interaction rate.

A system of LeCroy 1440 power supplies supplied individually adjustable high voltages to the photomultiplier tubes. The 1440 system was controlled by a FORTRAN program running on a VAX 11/780 computer.

The anodes of the Active Converter and Main Array photomultiplier tubes were connected via coaxial cables with the inputs of a set of amplifier/ADC modules [7] built at Fermilab. The cables used were RG8U ~200 nsec in length, with shorter lengths of RG58 (up to ~80 nsec) and RG174 (up to ~4 nsec) cable used as patch cables and for relative timing adjustment. RG8U was chosen to minimize losses, dispersion, and noise due to the long cable runs. The high voltage cable associated with each photomultiplier tube was bundled as close as possible to its associated signal cable to minimize the area of the loop between them. The shields of the signal cables were grounded only at the inputs of the amplifier/ADC system, to avoid ground loops.

The amplifier/ADC system resided in three modified CAMAC crates, two for the Main Array, and one for the Active Converter. The Main Array crates contained 13 amplifier-ADC modules each, and the Active Converter crate contained 8 modules. Three of the input channels in one of the Active Converter modules were used to instrument the PIN diodes associated with the LED pulser system described in Section 3.4.

Each module of the amplifier/ADC system had 16 input channels, each of which continuously integrated the charge pulses coming from a single block. The output voltage for a

given integrated charge was determined by the choice of integrating capacitor. A resistor in series with the integrating capacitor minimized the rise time of the integrating amplifier output. The 16 integrated signals on a module entered individual 400 nsec packaged delay lines.

A difference amplifier continuously subtracted the delay line input voltage from the voltage at a 160 nsec tap on the delay line. The difference amplifier output was a train of monopolar pulses ~160 nsec wide, whose amplitudes were proportional to the energy deposited in the block by particles from each interaction in the experimental target. The sixteen analog energy pulses from each Main Array amplifier/ADC module were sent to a set of TDC's and to a trigger processor [8].

A single Charge Controller Card in each crate received triggering pulses just before and just after the integrated charge from an interaction of interest appeared at the delay line output, and distributed these pulses to all of the channels in a crate. The "before" and "after" pulses opened JFET electronic switches to a pair of sample-and-hold capacitors.

The differences between the before and after capacitor voltages for the 16 channels on each module were amplified and digitized in pipeline fashion by a single ADC, so that the digitized value from each channel represented the energy in the channel from the interaction of interest. The after-minus-before analog value from each channel was sampled before presentation to the ADC input; if the value was less than 1/8 of the voltage corresponding to the full scale of the ADC, the analog input was multiplied by 8 before digitization, enhancing the energy resolution at the lower end of the dynamic range.

Each word from the amplifier/ADC system consisted of 16 bits: 12 bits corresponding to a single block energy, a single bit indicating whether the x8 multiplication had been performed, and 3 bits coarsely digitizing the integrated energy in a block just before the interaction of interest. These latter three "before bits" were used off-line, to help correct for a shift in the measured baseline digitized outputs, as described in Section 4.7.

3.2 Position Hodoscope Electronics

Signals from the LGC and GTH were too small to transmit to the digitization electronics without amplification, and so a system of analog amplifiers were mounted directly on the sides of

the LGC and GTH planes. Signals from the LGC tubes and stripes were amplified 5x and 25x respectively. The GTH tubes and stripe signals were amplified 20x and 25x respectively.

52 Ohm RG8U cables 200 nsec in length (and some shorter lengths of RG58 50 Ohm cable) transmitted the amplified signals to a system of LeCroy 2285 12-bit ADC's. The ADC's were controlled by LeCroy 2280 controllers, which allowed them to be read out in so-called sparsified mode. In this mode, a set of pedestal values were loaded before data taking. Only information from channels whose digitized outputs exceeded their pedestal values by a preset threshold were written to tape. This technique had the advantage of reducing the number of words that had to be written to tape for an event. However, pedestals and thresholds had to be carefully monitored during running, to make sure that information was not being lost due to pedestal drifts. Pedestals were determined by taking special triggers when beam induced interactions were not taking place. The pedestals were updated and loaded at least once daily.

3.3 Glass TDC System

One of the analog energy outputs from each Main Array block was split and sent to a simple energy summing trigger and to a system of LeCroy 4290 TDC's [9]. The TDC's were run in common STOP mode. The START time for a channel was determined by the time at which the analog energy pulse from the corresponding glass ADC channel rose above a threshold. The master trigger gate from the experiment supplied the common STOP signal.

3.4 LED Pulser System

Calibrations of the entire calorimeter were done about once per month of running. Each calibration established gains and pedestals for all channels of the Main Array, Active Converter, and LGC as explained in Section 4 of this paper.

Changes in the temperature of the photomultiplier tubes and electronics, glass degradation due to radiation damage, and magnetic field changes could all cause long and short term variations in the gains and pedestals of the glass block channels. To correct for these changes off-line, a precision LED pulser system was devised [10, 11].

The system delivered light pulses of nearly constant intensity to all glass blocks using a set of LED's. The light was generated by 96 green HP HLMP-3950 LED's driven synchronously by 10 A current pulses with 100 nsec width. The LED circuits were mounted on printed circuit boards, four channels per board. Each channel had a 6200 pF capacitor, and the 96 capacitors were charged by a common DC high voltage supply to 160 V through 150 kOhm resistors. The printed circuit boards were housed in an aluminum box, to shield the outside as much as possible from high frequency noise generated by the large current pulses. Individual glass fibers were attached to each of the 96 LED's. The ends of these fibers were brought together into a single bundle.

A separate distribution fiber bundle assembled by Fiberguide Industries allowed the transmission of the LED light to the individual glass blocks. The distribution bundle consisted of 200 fibers 7 m in length with .06 cm diameter and 500 fibers 8 m in length with .03 cm diameter. The distribution bundle was held at one end by a stainless steel sheath, and fanned out at the other end into three smaller groups of fibers; one group went to the Main Array front, another to the Active Converter, and a third group of 15 fibers with .06 cm diameter fibers went to three PIN diodes used to monitor the LED light intensity. The Main Array bundle contained .06 cm diameter fibers for the SCG1-C blocks, and .03 cm diameter fibers for the SF5 blocks. The Active Converter group contained all .03 cm diameter fibers. The fibers were inserted and glued into glass prisms epoxied to the block faces, so that light was directed toward the photomultiplier tube. To make it possible to vary the intensity of the light delivered to the glass blocks, the Filter Wheel, a carousel with twelve windows at its perimeter, was placed between the 92-fiber bundle and the distribution fiber bundle. Ten of the Filter Wheel windows held neutral density filters of varying opacity; the other two were open and opaque respectively. Table 2 shows the percentage of light transmitted by each of the windows.

The Filter Wheel was controlled from the same Motorola VME/10 computer that controlled the glass table motion. The position of the Filter Wheel was known through a system consisting of holes in the wheel, LED's, and light sensors, which established a four-bit word which was sent to a CAMAC input register read out by the data acquisition system.

For test purposes, the LED's could be triggered by a 100 Hz free-running oscillator. During normal data taking, the LED's were triggered by a coincidence of signals from a 60 Hz oscillator (prescaled by a factor of 32 to make 1.875 Hz), a signal from the accelerator clock that indicated the accelerator was between spills (so that no energy from interactions was being deposited in the calorimeter), and a "strobe" signal from the Filter Wheel control electronics that indicated the Filter Wheel was at a stable location.

During normal data taking, the VME/10 computer put the Filter Wheel through a repeating sequence of positions, 1, 8, and 12. The position was changed during each spill. Data taken with the filter wheel in position 1 (0% transmission) established the "pedestals" for the glass electronics. (A pedestal is the digitized pulse height present in a channel when no energy has been deposited.) Position 12 data (100% transmission) were used to determine gain corrections, as described in Section 4.6 of this paper.

3.5 Hardware Pedestals

Each channel of the calorimeter had a hardware pedestal, some number of digital counts corresponding to zero deposited energy. These pedestals were generally well-measured quantities. All Main Array and Active Converter blocks had their pedestals measured between beam spills throughout the running period, and the LGC and GTH pedestals were measured several times a day throughout the run. All energy variables in the following discussions have had these hardware pedestals subtracted as a first step before the application of gain factors which convert ADC counts to energy.

4. CALIBRATION PROCEDURE

The calorimeter was calibrated seven times during the data taking period, as shown in Table 3. In general, each calibration employed a series of electron or positron beams of known momenta to establish gains of all channels in the calorimeter.

4.1 High Voltage Setting

The maximum digitizable shower energies chosen for the three types of Main Array glass block were 200 GeV/c^2, 150 GeV/c^2, and 100 GeV/c^2 for the small SCG1-C, large SCG1-C, and SF5 blocks, respectively. Once these values had been chosen, the energies corresponding to a least digital count for a given block (and by implication the desired number of digital counts for a 30 GeV/c calibration beam) were fixed for the three block types. Before the actual calibration, the high voltages of all Main Array blocks were set one at a time. This was done by centering a 30 GeV/c beam on each block, and then adjusting the high voltage of the block until its digitized signal had the value corresponding to the mean energy deposited in the block as predicted by the EGS-IV Monte Carlo [12].

When the analyzing magnet was turned on after calibration, the high voltages had to be reset to correct for the effects of the magnet fringe field. This effect could be large for some blocks; the front and back Active Converter responses to the LED pulser were degraded by 10 to 70 %, and the Main Array large block responses by as much as 20 %. To do this, the high voltage of each block was adjusted to make the block's response to the LED pulser with the analyzing magnet turned on equal to its response with the magnet off.

4.2 Beam Energy Determination

Before a calibration was performed, the beam line devices were tuned to accept the desired momentum. The lithium target was removed from the beam, and data were taken with the analyzing magnet turned on, so that the momentum of the beam could be determined using the proportional wire chambers and drift chambers of the Experiment 705 spectrometer. To insure that the beam traveled through live regions of all drift chambers and proportional wire chambers (the central regions of all chambers were deadened to avoid saturation in high rate running), it was necessary to shift the beam some distance from its normal horizontal position.

Figures 7a-d show momentum distributions from a set of 6, 10, 30, and 60 GeV/c calibrations. Evidence of bremsstrahlung is present in all four figures. It is highly unlikely that

this bremsstrahlung was present in the calibration data taken with the beam in its normal undeflected condition; rather, it was due to the beam striking some material only when it was shifted horizontally to avoid the deadened regions of the chambers. There is unfortunately no way of determining this from the existing calibration data, however. The bremsstrahlung degraded the determination of the calibration beam momenta somewhat; however, the absolute energy scale of the calorimeter was ultimately set by quantities observed in the actual data, such as the π^0 mass and the ratio of E/p for tracked electrons and positrons from pair conversions of photons.
After the calibration sequence described in the next section had been performed at a given momentum, the momentum determination was repeated, to see whether beam line conditions had changed from the start of calibration to the finish.

Pion contamination in the calibration beams varied between about 3% at the lowest momenta to about 50% at 100 GeV/c. Two threshold Cerenkov counters were used to prevent pions from producing calibration triggers. The pion contamination in the final sample of calibration events was estimated to be less than 1%.

4.3 On-line Calibration Procedure

Once the calibration beam energy had been measured, the analyzing magnet was turned off, and the beam was centered in the spectrometer aperture. A program was then run on a Motorola VME/10 computer, which moved the glass table through a preset sequence of positions, allowing beam to enter each block of the Main Array, as shown in Figure 8. In general, 1000 events were written to tape for each main array block before the program moved the table to the next position, although typically about 20% of these events had to be rejected because of the presence of multiple beam tracks. For the Main Array blocks behind the LGC, the table was positioned so that the beam was centered on the target block. For blocks in the Active Converter region, the beam was centered on an Active Converter block in front of the target block, so that the Main Array blocks in this region were calibrated with beam 3.25 cm to the left or right of center.

The on-line procedure took several hours. As many as two blocks could be done per 23 second spill, with ~50 sec between spills. The entire data sample for one calibration energy could

be placed on several 9-track 6250 BPI magnetic tape reels. The on-line calibration procedure is described in more detail elsewhere [11].

4.4 Off-line Calibration Analysis: 30 GeV/c Data

The off-line calibration analysis determined gain constants for Active Converter, LGC, and Main Array channels by minimizing the width of the observed energy spectrum of calibration electrons [13]. In practice, the analysis was run only on the 30 GeV/c data from the various calibrations. The procedure was iterative, using starting values for all gains determined by the high voltage settings described in Section 4.1.

In general, the gain of a channel k of the Main Array, Active Converter, or LGC is defined by the expression

$$E_k = G_k * P_k \qquad (4.4.1)$$

where G_k is the gain, P_k is the pulse height in digital counts (with a pedestal subtracted if necessary), and E_k is the energy in GeV/c^2.

Each iteration of the main loop represented a loop over all table positions in the calibration sequence. For the N_{evt} events from each table position (as mentioned before, N_{evt} was usually about 1000), new gain values were determined for the targeted Main Array block and up to two Active Converter blocks (one in the front and one in the back Active Converter rows) or the LGC planes in front of the targeted Main Array block.

Individual LGC tube relative gains were determined in a separate procedure. The channel corrections were obtained by smoothing the summed pulse height distributions over the LGC for a large sample of interactions, based on the hypothesis that on average, the energy from interactions should be distributed continuously over the active area of the LGC. The GTH pulse heights were corrected by a smoothing similar to that used in the LGC; however, no attempt was made to convert the corrected pulse heights to energies, since the GTH was used only for position reconstruction.

Equations for the total measured energy E_T in three distinct regions of the detector may be written as follows:

$$E_T = \Sigma_{clus} G_m P_m \tag{4.4.2}$$

$$E_T = \Sigma_{clus} G_m P_m \quad + G_{LGC} \Sigma_{LGC} G_l P_l \tag{4.4.3}$$

$$E_T = \Sigma_{clus} G_m P_m + \Sigma_{ACfr} G_a P_a + \Sigma_{ACba} G_b P_b \tag{4.4.4}$$

The first sum in each equation is over the targeted Main Array block and its nearest neighbors. Equation 4.4.2 applies to the outermost columns of the Main Array, with no Active Converter blocks in front. Equation 4.4.3 applies to the region of the Main Array covered by the LGC. The second sum in this equation is over the set of LGC tubes in front of the targeted block. G_l are individual relative tube gains, and G_{LGC} is an overall x-plane gain for the LGC region in front of the targeted Main Array block. Equation 4.4.4 applies to the region of the Main Array covered by the Active Converter. The second and third sums are over the targeted front and back Active Converter blocks and their two nearest neighbors. (For Main Array positions near y = 0, sums over six Active Converter blocks were used.)

The gain parameters for the targeted Main Array block and front and back Active Converter blocks or LGC tube were determined by minimizing the quantity

$$\Sigma_{N_{evt}} (E_{beam} - E_{T_i})^2 \tag{4.4.5}$$

where E_{beam} is the calibration beam energy, and E_{T_i} is the total measured shower energy of the ith event out of the sample of N_{evt} events recorded at the table position.

This fitting procedure produced a distinct active plane gain constant at the position of each Main Array block; far more than the number of unique active plane elements. Consequently, we defined a gain for each active element that would reproduce the EGS-IV prediction of the mean energy deposit in that element, then interpreted the surplus in each fitted gain as being a longitudinal shower development correction to the energy in a Main Array block. On a grid of the main array blocks this process also corrected for any residual positional gain variations within an active element, but the corresponding energy was incorrectly assigned to the main array rather than to the active plane.

In addition to the gain, a parameter was extracted for each Main Array block which took into account variations in longitudinal shower development as reflected in the division of energy between the Main Array and Active Converter (or LGC). The expression

$$E_T = E_M + (1+b_m) * E_A \qquad (4.4.6)$$

gives the corrected total shower energy E_T in terms of the measured Main Array energy E_M, the measured Active Converter or LGC energy E_a, and the correction factor b_m.

The Active Converter column energies E_a were corrected for attenuation along the long axis of the blocks by fitting for two parameters D_0 and n in addition to the gain G_a such that

$$E_a = (D + D_0)^n G_a P_a \qquad (4.4.7)$$

where D is the distance from the phototube end of the block at which energy is deposited. Since each Active Converter column was used to calibrate three Main Array blocks corresponding to three different values of D, the parameters D_0, n, and G_a could be uniquely determined. A further requirement was imposed, namely that the average Active Converter energy must be equal to that predicted by the EGS-IV Monte Carlo program.

4.5 Calibration Momenta Other than 30 GeV/c

The 30 GeV/c calibration data were chosen for detailed analysis described in the previous section because they optimized transverse beam shape, compact shower profiles in the glass, and narrow beam energy spectrum. To account for variations in the calibration constants with shower energy, two energy-dependent parameters were defined for each Main Array glass block type. The total energy of a shower in a block i may then be represented by

$$E_T = \alpha_i * E_A + \beta_i * E_M \qquad (4.5.1)$$

where α_i and β_i are both defined to be unity at the momentum 30 GeV/c. For each of the other calibration momentum values, α_i and β_i were determined so that the width of the measured energy spectrum was minimized while preserving the mean energy.

The final analysis code first calculated the Main Array and Active Converter (or LGC) energies of a shower using the calibration constants from 30 GeV/c data. It then made the longitudinal correction as shown in equation 4.4.6. Finally, the code interpolated in a table of α_i

and β_i as measured at the various calibration energies for block i, and calculated the final shower energy from equation 4.5.1.

4.6 Gain Tracking

The calibration algorithm described in Section 4.4 determined gains at each 30 GeV/c calibration. Various time-dependent shifts in glass block gains affecting the data taken between calibrations were corrected in each event using the LED pulser data.

For each event, the pedestal-subtracted pulse height in a block was corrected using the ratio of the block's current LED open Filter Wheel response p_{12now} and the LED open Filter Wheel response at the time of calibration $p_{12calib}$, as well as the PIN diode responses to the LED flash at the time of the event and the time of calibration, PIN_{now} and PIN_{calib}:

$$P_{corr} = \quad P_{raw}*(p_{12calib}/p_{12now})*(PIN_{now}/PIN_{calib}) \qquad (4.6.1)$$

The first term in parentheses corrected for changes in the block response, the second for changes in the light level of the LED pulser system.

Comparison of data for two calibrations approximately one month apart yielded an upper limit of 1.0 % in the tracking error of the block gains [11]. That is, the gain calculated using the LED and PIN diode response information is distributed about the true gain value with a standard deviation of less than 1.0%.

4.7 Rate Dependent Pedestal

During a small portion of the running we ran the LED flasher during the normal beam spill to produce no-light pedestal triggers; during most of the running these pedestal triggers were produced only between spills. The out-of-spill triggers showed a very narrow pedestal associated with noise in the ADC itself, but the in-spill pedestal showed a large and broad additional pedestal, particularly in the SCG1-C glass. The average value of this pedestal in a particular block was found to be strongly correlated with the mean energy deposited in that block by minimum bias triggers, varying with the interaction rate, the cross-sectional area of the block, and the block's distance from the beam path. Figure 9a shows the ratio of the pedestal to mean deposited energy for each block in the detector. There are three distinct block groupings on this plot corresponding

to SF5, large SCG1-C, and small SCG1-C. The points for the SF5 blocks are widely scattered because the rate-dependent pedestal is quite small in these blocks as a consequence of their small mean energy deposit. Figure 9b shows the pedestal width plotted against the mean deposited energy.

Review of the ADC electronics revealed a subtle feedback path that was highly sensitive even to DC levels from the photomultiplier tubes. It is therefore believed that this rate-dependent pedestal is caused by a residual glow in the glass caused by the showers from untriggered events immediately preceding a triggered event.

In this model, the observed width of the pedestal results from statistical fluctuations in the number and size of showers that develop in a particular block prior to a triggering event. Thus, at high rates, the signal from both SCG1-C and SF5 glass appears to contain a large low frequency background component that would be difficult to eliminate with any single sampling ADC. In this experiment we have no way to reduce the pedestal width, but by using the correlation between the average energy deposit in a block and its pedestal mean we are able to remove most of the offset. The average energy deposit in a block is a function of beam x, y position which changes only occasionally and the instantaneous interaction rate which varies with beam intensity during a spill and for a variety of reasons on the longer term. To control for changes in the beam position, we averaged over minimum-bias triggers to make maps of the mean energy deposit as a function of block number, but in the bulk of our data our only way of estimating the instantaneous interaction rate was to interrogate the "before-bits" discussed in Section 3.1.

In our sample of in-spill pedestal triggers, we observed a correlation between each block's pedestal and a sum-over-blocks of the "before-bit" information contained in that event. For each block, this correlation was fit to a linear function, producing slope and intercept constants a and b that we used to describe the rate dependence of each block's pedestal.

These mean energy maps and the before-bit estimate of the instantaneous interaction rate were used to extrapolate the observed rate-dependent pedestal to the bulk of our data using the pedestal formula

$$P = P_0 + \langle E \rangle [aB + b] - \langle E_0 \rangle [aB_0 + b] \qquad (4.7.1)$$

where P_0 and B_0 are respectively the mean energy and mean before-bit energy observed for in-spill pedestal triggers, $\langle E_0 \rangle$ is the mean energy deposit by minimum bias triggers in the same tapes, while $\langle E \rangle$, B, and the resulting pedestal P are similar quantities for a different data sample. All quantities in this formula except B and B_0 are block dependent.

5. EVENT RECONSTRUCTION

A comprehensive algorithm was developed to reconstruct the 4-momenta of photons produced in interactions by measuring their energies and positions in the calorimeter. The algorithm also reconstructed particles other than photons, including electrons and positrons as well as some hadrons. Hadrons were imperfectly reconstructed since in general they deposited only a small fraction of their energy in the calorimeter.

The reconstruction algorithm had to deal with overlapping showers, two or more of which could contribute energy to a given channel. An iterative energy-fitting/position-locating/block-energy-sharing procedure was developed to partition the energy in a block between a set of contributing showers.

More detailed discussions of the shower reconstruction algorithm may be found elsewhere [9,11,13,14,17].

5.1 Energy Arrays

The first step in the reconstruction of an event was to fill deposited energy arrays for the Main Array blocks, the Active Converter blocks, and the LGC tubes and strips. A similar array was also kept for the GTH channels, but its contents were simply relative pulse heights with no energy conversion.

5.2 Cluster Definition

A Main Array cluster was defined by a central peak block that contained more deposited energy than was present in the blocks on any of its four sides. The typical cluster consisted of nine blocks although clusters on the large-block small-block boundary could contain ten or eleven

blocks. The energy in the peak block was required to be greater than 300 MeV/c^2. This definition allowed the peak blocks of two clusters to touch at a common corner.

Blocks associated with a single cluster had their full energy assigned to it, but blocks associated with more than one cluster had their energy divided between the clusters. The initial division of energy was proportional to the peak block energies of the clusters sharing the block. The total cluster energy was initially defined as the sum of the assigned energies of all blocks contained in the cluster, and the initial cluster position was taken to be the center of the peak block.

5.3 Cluster Position and Energy Determination

A sample of electromagnetic showers generated by the EGS-IV simulation was used to produce tables from which we reconstructed the position and energy of each main array cluster. Three types of particles were simulated separately: 1) photons entering the calorimeter as if they had been produced in the target, 2) electrons of normal incidence (to simulate calibration events), and 3) electrons entering the calorimeter with an angle which depended on their momentum and position.

As indicated in Figure 10, tables were generated for both the normalized shower shape quantities p_i and the position estimators r_{ij}. To keep both tables manageable, we assumed that the two dimensional shower shape could be represented by uncorrelated x and y distributions and generated entries only for three blocks oriented parallel to the +x axis in the first quadrant of the detector. We then used exact and approximate symmetry properties to modify these tables for the y patterns and for the other quadrants. Since the magnetic field breaks the azimuthal symmetry for deflected electrons, the table entries for deflected photons were used for the y patterns of particle type (3) above. Table entries were generated for twenty x positions relative to the center of the peak block, eight x locations in the glass block array, two azimuthal angles around the beam direction, five logarithmically distributed energies, and four mean shower depths. A table of the variance of each entry was also kept.

A position for each cluster was calculated using an inverse variance weighted average of the r_{ij} appropriate for the shower. In the absence of background energy or shower sharing, the

best energy estimate for a shower is clearly obtained from a simple sum of the measured energy in each block of a cluster. However, for our non-calibration data we found that a fitting procedure gave a better estimate of the actual shower energy.

Based on initial estimates of the energy and position of a shower, we began the fitting process by extracting a unity-normalized predicted nine-block shower shape S_i from the tables. The corner blocks (6:9 in Figure 10) were not given directly by the tables, but were estimated from empirical extensions to the expression $S_{corner} = S_i\, S_j/S_k$, where blocks i and j share common boundaries with the center block k and the corner block.

A fitted energy for each cluster was determined by minimizing the quantity

$$\chi^2 = \Sigma_{ij}(E_i - A\mathcal{S}_i)\, M_{ij}\, (E_j - A\mathcal{S}_j) \qquad (5.5.1)$$

with respect to the scale factor A. In this expression, the E_i are the block energies assigned to the cluster, the $\mathcal{S}_i$ are the predicted energies from the pattern tables, and M_{ij} is the inverse covariance matrix. We approximated this matrix with the expression

$$M_{ij} = E_iE_j / [\sigma \max(E_iE_j)]^2 \qquad (5.5.2)$$

when i and j are neighboring or repeated blocks, and zero otherwise. This form puts $1/\sigma^2$ on the diagonal and approaches this value as the energy deposited in two neighboring blocks becomes identical, but minimizes the related off diagonal terms when the energy in one block is much larger than the other [14]. The quantity σ was used for chi square normalization purposes and was derived from the table variance entry for the central block.

For each cluster in the event, the energy fitting was repeated in the overall iteration loop a maximum of 25 times, or until all block energies were within 1% of their values from the previous iteration. After each iteration, the "fractional energy error" F for each cluster was calculated:

$$F = \sqrt{(\Sigma_i(E_{out} - E_{in})^2)} \,/\, \Sigma_i(E_{out}) \qquad (5.5.3)$$

where the sum runs over the five blocks used to form the patterns discussed above. E_{in} are the energies going into the iteration, and E_{out} are the energies after the iteration. Together with the chi square, this quantity was useful for estimating the quality of a shower's energy determination.

5.4 Position Determination Using the LGC and GTH

Positions of showers were determined by examining the energy deposited in the horizontal and vertical views of the LGC and GTH. Peaks corresponding to electromagnetic showers were located in the energy and pulse height profiles of the LGC and GTH respectively using a deconvolution technique. A predicted shower shape was deconvoluted from the measured profiles, and the resulting distribution was scanned for channels above a certain threshold. This technique proved superior to a simple peak search algorithm in resolving overlapping showers and was able to return a satisfactory LGC energy without further need to separate showers [13]. A gaussian digital filter was also applied in the offline analysis of the hodoscope data to eliminate noise due to low particle statistics in the early part of the shower. This was particularly important in the GTH [9].

For each cluster in the Main Array, a search window was defined about the position as obtained from the glass information, with dimensions ±3 times the calculated position uncertainty. The maximum and minimum dimensions of the window were ±6 cm and ± 3 cm respectively. Hodoscope peaks lying within the horizontal and vertical search windows of a cluster were matched using an asymmetry parameter defined as

$$\alpha = (E_x - E_y) / (E_x + E_y) \qquad (5.5.4)$$

A cut was imposed on this parameter, demanding that α be less than 25% in the LGC or 35% in the GTH. These values were chosen by examining asymmetry distributions for showers from calibration electrons. If a pair of peaks passed the asymmetry cut, they formed a potential "hodoscope crossing". Attempts were also made to match two peaks in one view with a single peak in the other view. If multiple crossings were found within a cluster window, the pair with the smallest asymmetry value was chosen. If a hodoscope crossing was found, the final position of each cluster was defined as the weighted average of the positions determined by the glass information and by the GTH or LGC.

6. PERFORMANCE

The performance of the Experiment 705 calorimeter has been assessed by examining energy resolution, position resolution, and reconstruction efficiency for electromagnetic showers

both in calibration data and in high intensity interactions. Stability over time and uniformity over the active region of the detector are also important aspects of the energy scale. Each of these performance criteria are examined in the following sections using samples of electron/positrons, π^0's, and η^0's reconstructed from high-rate data.

6.1 Energy Resolution and Energy Scale

The fractional energy resolution $\sigma(E)/E$ is usually parameterized as

$$\sigma(E)/E = \alpha + \beta/\sqrt{(E)} \qquad (6.1.1)$$

where the quantity α reflects uncertainty in the energy scale from shower to shower due to variations in gain parameters and other systematic effects, and the β term represents the effect of sampling fluctuations, which dominate the energy uncertainty for most showers in this experiment. A third term, proportional to 1/E, is sometimes added to the expression, to account for random fluctuations in pedestal due to electronic noise. At calibration beam intensities, the contribution to the energy resolution from random pedestal fluctuations was very small [7], so that the addition of a term in 1/E was not necessary. Because we observe an interaction rate dependent pedestal in this experiment, it is necessary to consider the behavior of $\sigma(E)/E$ for calibration and high-rate running separately.

6.1.1 Calibration Data

As explained in Section 4.4, the gains determined by the off-line calibration algorithm minimized the width of the energy distribution at a given calibration energy. The energy resolution $\sigma(E)$ could then be extracted from these widths. Table 4 shows $\sigma(E)$ for four of the calibration beam momenta in the various regions of the calorimeter. The estimated momentum spread of the calibration beams, 0.7%, has been subtracted in quadrature. The values shown are from Gaussian fits to the energy distributions at the various calibration momenta.

The 2 GeV/c and 100 GeV/c calibration data were not used in this analysis. For the 100 GeV/c data, the pion contamination was large and an overflow condition sometimes occurred in the LGC. For the 2 GeV/c data, $\Delta p/p$ was large and the beam spot at the calorimeter front face was comparable to the dimensions of a large glass block, complicating the calibration analysis.

The values for $\sigma(E)/E$ determined from the values of $\sigma(E)$ in Table 4 are fairly linear in the quantity $1/\sqrt{(E)}$. Values for the intercepts and slopes of a staight line fit are given in Table 5 for the four regions of the detector.

The result for the large SCG1-C in the GTH/Active Converter region can be compared with a test result obtained at SLAC [15,16], $\sigma(E)/E = 0.64\% + 3.9\%/\sqrt{(E)}$. The somewhat degraded result for the Experiment 705 calorimeter is to be attributed in part to differences in position hodoscope construction for the GTH and SLAC test device, and to the 1.3 cm steel plus 0.8 cm lead radiator in front of the Experiment 705 Active Converter, which was not present in the SLAC test apparatus. The larger errors in the central region stem from the LGC energy resolution coupled with the shower depth sensitivity of the SCG1-C glass.

6.1.2 Electron-Positron Pairs in High-Rate Data

Pair conversions of photons in the lithium target provided a powerful tool for measuring the performance of the calorimeter in 300 GeV/c interactions. About 7% of the photons produced in the target converted into electron-positron pairs. One or both of the pair of particles could be tracked in the charged particle spectrometer. For a tracked electron or positron entering the active region of the calorimeter, the ratio of reconstructed shower energy to track momentum, E/p, should be close to unity due to the smallness of the electron mass.

In addition to the error in E, the momentum resolution of the charged particle spectrometer contributes to random deviations of E/p from unity. However, this contribution is expected to be small. For example, at 20 GeV/c the track momentum resolution $\sigma(p)/p$ was ~1.2%. Monte Carlo simulations taking into account multiple scattering and chamber granularity predict that for lower values of momentum, $\sigma(p)/p$ falls off parabolically, approaching a value of approximately 0.05% at zero momentum. However, there are other effects at very low momentum values (e.g., spiraling of tracks due to the small magnetic field components) which probably degraded the momentum resolution further. In any case, the contribution to the width of the E/p distribution from tracking was probably never greater than a few percent. We further note that the minimum momentum for tracks considered in this paper is about 4 GeV/c.

Electron and positron candidate showers were selected by requiring that a charged particle track point to within 3 cm of the measured position of a shower with at least 200 MeV/c^2 of energy in the LGC or Active Converter. The latter cut was intended to remove most of the hadrons, about 90% as estimated from charged pion test beam data [17].

Figure 11 shows $\sigma(E)/E$ as a function of $1/\sqrt{(E)}$ for the four detector regions. The triangles represent $\sigma(E/p)$ for electrons and positrons reconstructed in high rate data, while the circles show the fractional resolution $\sigma(E)/E$ for calibration beams obtained from the information in Table 4.

The energy resolution for high rate running is degraded relative to the calibration resolution. This is expected, since interactions produced by 300 GeV/c particles affect the reconstruction adversely in several ways. These include: 1) hadronic energy deposited in the calorimeter which is mistakenly associated with an electromagnetic shower, 2) energy from improperly reconstructed electromagnetic showers which overlap the shower of interest, and 3) imperfect correction of the pedestal shift discussed in Section 4.6.

6.1.3 π^0 and η^0 Decays in High Rate Data

Di-photon mass combinations were examined in the π^0 (135 MeV/c^2) and η^0 (549 MeV/c^2) mass regions. Photon shower candidates were selected for the π^0 analysis by making the following requirements: The shower position was measured by the LGC or the GTH. The ratio of energy measured in the LGC or Active Converter to the square root of the total energy (both energies in GeV) was greater than 0.15. The shower fitting χ^2 was less than 10. The fractional energy error parameter ΔE_f was less than 0.2.

Figures 12a-e show invariant mass distributions for various photon energy ranges. Clear π^0 signals are seen in all five plots. In each case, the superimposed function is a Gaussian plus a 3rd order polynomial.

Table 6 shows the measured values of the π^0 central mass and mass resolution (the mean and sigma of the best fit Gaussian function) for the four regions of the detector. The values are all within about 3% of each other.

Showers for η^0 studies were required to satisfy the following requirements: The shower position had to be measured by the LGC or GTH. No charged track pointed to within 5 cm of the shower center. The shower energy was greater than 5 GeV, and the summed energy of both showers was greater than 15 GeV. The shower fitting χ^2 was less than 0.4, and the fractional energy parameter ΔE_f was less than 0.15.

Figure 13 shows the photon - photon mass distribution in the η^0 mass region. A clear η^0 signal is seen. The fitted mass is 556 ± 4 MeV/c^2, with sigma = 17 ± 4 MeV/c^2. The central mass is within 3% of the true η^0 mass, indicating again the accuracy of the Experiment 705 energy scale at the level of a few percent.

6.2 Position Resolution

Shower position resolution contributed to the uncertainty in the four-momenta of photons, and therefore to the mass resolution of photon - photon combinations, as seen above for the π^0 and η^0.

The position resolution was measured using calibration electrons as well as electrons and positrons produced in high rate running. The calibration electrons were tracked in beam chambers upstream of the target and extrapolated to the calorimeter, and the produced electrons were tracked in the downstream chambers. The position resolution was obtained by comparing the predicted impact locations with the shower positions determined by the electromagnetic shower reconstruction algorithm.

6.2.1 Calibration Data

The open circles on Figures 6.4a-e indicate the sigmas of the residual distributions between the extrapolated beam track position and measured shower position for calibration electrons in the various detector regions. The numerical results are shown in Table 7. Given that the spectrometer tracking chambers were desensitized in the beam region, we have no independent measure of the quality of the beam track extrapolation in calibration data, but because of possible multiple

scattering in the mirrors of the beam Cherenkov counters we are most confident of the higher momentum measurements.

6.2.2 Produced Electrons in High Rate Data

A subsequent study using produced electrons and positrons found by the tracking program yields the position resolutions shown by the open triangles in Figure 14. Comparison with the calibration beam data (shown by open circles in Figure 14) indicates substantial uncertainty in the extrapolated locations at the calorimeter for low energy calibration beams. These studies were done in a portion of our data when the LGC ADC's were overflowing on a fraction of high energy showers: this probably accounts for the slight degradation in LGC resolution with increasing energy. The worse resolution indicated in the LGC y-plane measurements is probably caused by larger downstream tracking errors (U,V planes were used) but since the induced y showers were broader than x showers, backgrounds from other showers may also be significant.

The position resolutions for electrons and positrons in standard (non-calibration) data, averaged over all observed momenta, are given in Table 8 for the various detector regions. For the LGC region, the position residual distributions were non-gaussian, and so the sigmas reported in Table 8 are obtained by converting the FWHM for the distributions into a sigma.

6.3 Reconstruction Efficiency

In general, the reconstruction efficiency for electromagnetic showers is a function of the energy and impact position of a particle entering the calorimeter. It is sensitive to the boundaries within the Main Array and active planes, dead spots, and unresolved overlapping showers, from both in-time and out-of-time events.

Tracked electron/positron pairs proved to be our best estimator of the reconstruction efficiency of the calorimeter. As mentioned in the preceeding sections, such pairs were copiously produced in the data, and fairly easily identified. The strategy was first to identify two tracks from a possible pair conversion, then require that one of the tracks be identified as an electron or positron using information from the calorimeter. If the other track entered the active area of the

calorimeter, the reconstruction efficiency could be assessed by asking how often an electromagnetic shower with the correct energy could be associated with this track.

Relying on pair conversions has the drawback that the impact positions of electrons on the calorimeter are strongly correlated with their momenta, so that it is not possible to determine the reconstruction efficiency over a large range of energies at a given position in the calorimeter. Electrons and positrons from pair conversions also tend to strike the calorimeter at vertical coordinate values close to the vertical beam coordinate, since the analyzing magnet only bends tracks to the left and right.

To identify charged tracks from photon conversions, opposite sign track pairs were selected having $(y^+ - y^-)$ less than 10 cm, where y^+ and y^- were the vertical positions of the positively and negatively charged tracks at the calorimeter face. This cut enhanced pair conversion selection, since the analyzing magnet only bent charged particles horizontally, so that two initially collinear particles would continue to travel in the same vertical trajectory. Both charged tracks were required to enter the active region of the calorimeter. Figure 15 shows the invariant mass for such track pairs. The peak below about 10 MeV/c^2 is due to photon conversions in the lithium target and surrounding material.

Identified photon conversion track pair candidates were then required to have at least one track satisfying the shower requirements given in Section 6.1.2 for an electron candidate. The shower reconstruction efficiency was then investigated by searching for a shower in association with the partner track. Figures 6.6a-d show the fraction of the time, plotted separately for each of the four major detector regions, that the partner track gave rise to a fully reconstructed electromagnetic shower. This ratio may be interpreted as the uncorrected reconstruction efficiency.

A correction factor must be applied to the reconstruction efficiency shown in Figures 6.6a-d, to account for falsely identified electron - positron pairs. This factor was evaluated in two different ways: First, opposite-sign track pairs from *different* events were checked, to see how often a pair passing the requirements was found. Second, *same-sign* track pairs from the same event were checked in the same manner. These techniques gave 8 ± 1 % and 14 ± 1% for the

estimated percentage of falsely identified pairs. Table 9 gives the uncorrected and corrected reconstruction efficiency averaged over momentum for the various regions of the calorimeter.

7. CONCLUSIONS

A large acceptance, highly segmented scintillating and lead glass calorimeter, with gas tube devices for position measurement, has been operated at high rate. Fractional energy resolution $\sigma(E)/E$ for calibration beams was measured to be

$$1.71 \pm .10\ \% + 11.83 \pm .43\ \%/\sqrt{E}$$

in SCG1-C scintillating glass with a lead-gas sampling active converter,

$$0.990 \pm .056\ \% + 4.58 \pm .22\%/\sqrt{E}$$

in SCG1-C glass with an SCG1-C active converter, and

$$0.331 \pm .018\ \% + 6.65 \pm .08\ \%/\sqrt{E}$$

in SF5 lead glass with an SCG1-C active converter. For 300 GeV/c interactions, the resolution is somewhat degraded from these values, as expected. Shower position resolutions were measured to be from 2 to 6 mm in all regions of the calorimeter for electrons and positrons in reconstructed in 300 GeV/c events. The reconstruction efficiency for electrons and positrons varies between 26% and 56% in the various regions of the detector. Having fixed the energy scale using reconstructed electrons and positrons from pair conversions of photons, we reconstruct π^0 and η^0 with the correct masses and good resolution. We find that our energy scale is stable at the level of ~3% across the active area of the detector and over the duration of the run, from August of 1987 until February of 1988.

ACKNOWLEDGEMENTS

The authors would like to thank the U.S. Department of Energy, the U.S. National Science Foundation, the Natural Sciences and Engineering Research Council of Canada, the Quebec Department of Education, and the Scientific Affairs Division of the North Atlantic Treaty Organization for their support of this experiment. We wish to acknowledge the assistance of the administration and staff of Fermi National Accelerator Laboratory, in particular the Physics Department Electronics Group, Research Services Electronic Support Group, Computing Division, and Lab 6 organizations.

REFERENCES

[1] Antoniazzi et al., "A Measurement of J/ψ and ψ' Production in 300 GeV/c Proton, Antiproton, and $\pi^{\pm}$ Nucleon Interactions. to be published in *Physical Review* **D**., and Antoniazzi et al., "Production of J/ψ via ψ' and ψ Decay in 300 Gev/c Proton and $\pi^{\pm}$ Nucleon Interactions, to be published in *Physical Review Letters*.

[2] Cox, B. et al., "A Measurement of the Response of an SCG1-C Scintillation Glass Shower Detector to 2-GeV to 17.5 GeV Positrons", NIM 219:487, 1984.

[3] Wagoner, D. et al., "A Measurement of the Energy Resolution and Related Properties of an SCG1-C Scintillation Glass Shower Counter Array for 1-GeV to 25-GeV Positrons", NIM A238:315, 1985.

[4] Cox, B. et al., "A Measurement of the Response of an SCG1-C Scintillation Glass Array to 4-GeV to 14-GeV Pions", NIM A238:321, 1985.

[5] Spiegel, L. et al., "Performance of a Lead Radiator, Gas Tube Calorimeter", IEEE Nuclear Science Symposium, Nov 9-11, 1988.

[6] Jenkins, C.M. et al., "Results from the E-705 Electromagnetic Shower Position Detector", IEEE Nuclear Science Symposium, Nov 9-11, 1988.

[7] Delchamps, S. et al., "Precision Charge-Sensitive Amplification and Digitization System for a Scintillating and Lead Glass Array", IEEE Nuclear Science Symposium, Nov 9-11, 1988.

[8] Zioulas, G. et al., "An On-Line Trigger Processor for Large Transverse Energy Events", IEEE Nuclear Science Symposium, Nov 9-11, 1988.

[9] Tesarek, R. J., "Hadroproduction of ^3P State Charmonium at $\sqrt{s}$ = 23.7 GeV", Duke University Thesis, 1993.

[10] Fortney, L. R., "An LED Source for Photomultiplier Gain Tracking." Calorimeter Calibration Workshop, 26-30 April 1983. Fermi National Accelerator Laboratory, Batavia, IL.

[11] Turkington, T., "Precise Measurement of Photons from the Interactions of 300 GeV/c Hadrons on a Lithium Target", Duke University Thesis, 1989.

[12] Nelson, W. et al., "The EGS-IV Code System", SLAC Report 265, 1985.

[13] Shen, Q., "High p_T π^0 and η Production by 300 GeV/c $\pi\pm$ and p Beams on a ^{7}Li Target", Duke University Thesis, 1992.

[14] Fortney, L. et al., "Shower Fitting Using a Covariance Matrix", submitted to NIM July, 1992.

[15] Rameika, R. et al., "Measurement of Electromagnetic Shower Position and Size with a Saturated Avalanche Tube Hodoscope and a Fine Grained Scintillator", NIM A242:215, 1986.

[16] Cox, B. et al., "High Energy Electromagnetic Shower Position Measurement by a Fine Grained Scintillation Hodoscope", NIM 219:491, 1984.

[17] Rosati, M., "A Measurement of Proton and Pion Induced P-Wave Charmonium Hadroproduction", McGill University Thesis, 1992.

	SCG1-C	SF5
Composition (by weight)	BaO 43.4% SiO2 42.5% Li2O 4.0% MgO 3.3% K2O 3.3% Al2O3 2.0% Ce2O3 1.5%	PbO 55% SiO2 38% K2O 5% Na2O 1%
Density	3.36 g/cm3	4.08 g/cm3
Radiation Length	4.25 cm	2.47 cm
Absorption Length (30-200GeV/c^2 pions)	45.6 cm	42.0 cm

Table 1. Properties of SCG1-C Scintillating and SF5 Lead Glass

Filter Wheel Position	% Transmission
1	0.0
2	0.1
3	0.2
4	0.5
5	1.0
6	2.0
7	5.0
8	10.
9	20.
10	50.
11	80.
12	100.

Table 2. Transmission Percentage for Various Positions of the LED System Filter Wheel

Date	Momentum (GeV/c)	Beam Sign
Jul 8-9, 1987	30 6 2	Negative
Aug 28-31, 1987	30 10 6 2 100 60	Negative
Oct 25, 1987	30a 30b	Negative
Nov 7-8, 1987	30 60 10 6 2	Positive
Dec 23, 1987	30	Negative
Jan 16-17, 1988	30 30b 6 100	Positive
Feb 9-12, 1988	30a 30b 60 10	Negative

Table 3. Calibration History of the Experiment 705 Calorimeter

	σ(E) (GeV)			
Detector Region	6.67 GeV/c	10.8 GeV/c	31.7 GeV/c	61.4 GeV/c
Small SCG	.442 ± .007	.542 ± .010	1.161 ± .020	2.100 ± .044
Large SCG (LGC region)	.399 ± .010	.498 ± 010	.879 ± .016	1.512 ± .027
Large SCG (GTH region)	.188 ± .004	.253 ± .005	.549 ± .011	1.028 ± .027
SF5	.198 ± .002	.255 ± .001	.433 ± .004	.775 ± .007

Table 4. Energy Resolution for Various Calibration Momenta and Detector Regions

Region	α (%)	β (% GeV1/2/c)
Small SCG	1.71 ± .10	11.83 ± .43
Large SCG (LGC region)	0.700 ± .082	12.83 ± .43
Large SCG (GTH region)	0.990 ± .056	4.58 ± .22
SF5	0.331 ± .018	6.648 ± .075

Table 5. Parameters in $\sigma(E)/E = \alpha + \beta/\sqrt{(E)}$ for Various Detector Regions (Calibration Data)

	Mean Mass (MeV/c^2)	Sigma (MeV/c^2)
Small SCG	138.4 ± 0.2	12.2 ± 0.3
Large SCG (LGC region)	137.9 ± 0.5	14.3 ± 0.6
Large SCG (GTH region)	142.5 ± 1.9	13.7 ± 2.0
SF5	137.6 ± 0.5	10.3 ± 0.5

Table 6. π^0 Measured Mass (Mean) and Mass Resolution (Sigma) for Various Detector Regions

	σ (cm)			
	6.67 GeV/c	10.7 GeV/c	31.6 GeV/c	61.4 GeV/c
LGC x	0.805 ±.004	0.494 ±.002	0.254 ±.001	0.233 ±.001
LGC y	0.805 ± .004	0.497 ± 002	0.232 ± .001	0.166 ± .008
single tube GTH x	1.077 ± .009	0.647 ± .005	0.365 ± 002	0.302 ± .002
double tube	1.139 ± .005	0.738 ± .004	0.487 ± .002	0.447 ± .002
single tube GTH y	1.064 ± .010	0.717 ± 006	0.406 ± .003	0.331 ±.003
double tube	1.076 ± .006	0.761 ± .004	0.398 ± .002	0.330 ± .001

Table 7. Position Resolution for Beams in Various Regions of the Calorimeter (Calibration Data)

	σ (cm)
LGC x	0.165 ± .003
LGC y	0.423 ± .008
single tube GTH x	0.494 ± .006
double tube	0.694 ± .005
single tube GTH y	0.655 ± .013
double tube	0.683 ± .013

Table 8. Position Resolutions for Electrons and Positrons in non-Calibration Data

Region	uncorrected efficiency (%)	corrected efficiency (%)
Small SCG	35 ± 3	40 ± 3
Large SCG (LGC region)	23 ± 2	26 ± 2
Large SCG (GTH region)	35 ± 2	40 ± 3
SF5	49 ± 1	56 ± 3

Table 9. Uncorrected and Corrected Average Electron Reconstruction Efficiencies

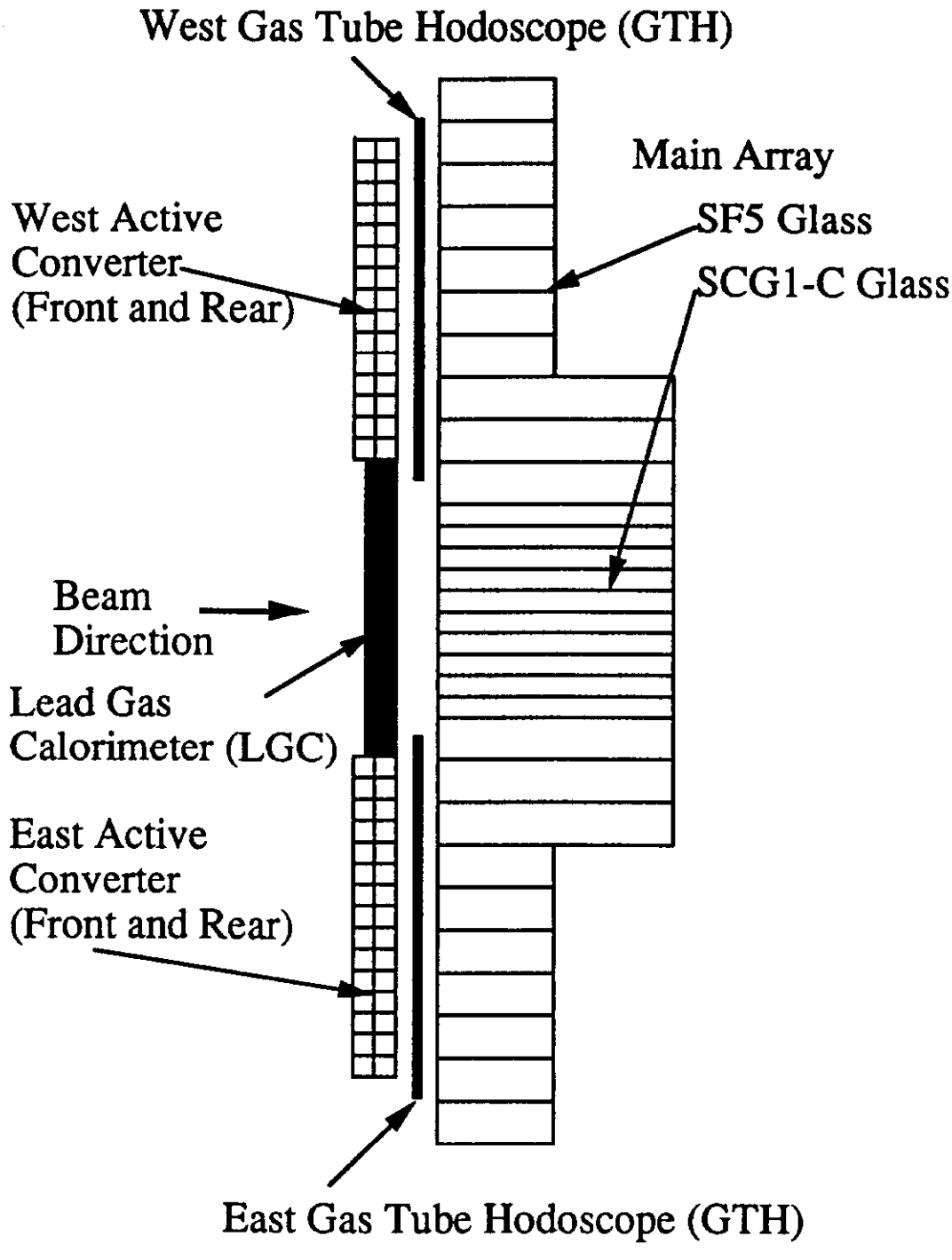

Figure 1. Plan view of the major components of the Experiment 705 calorimeter

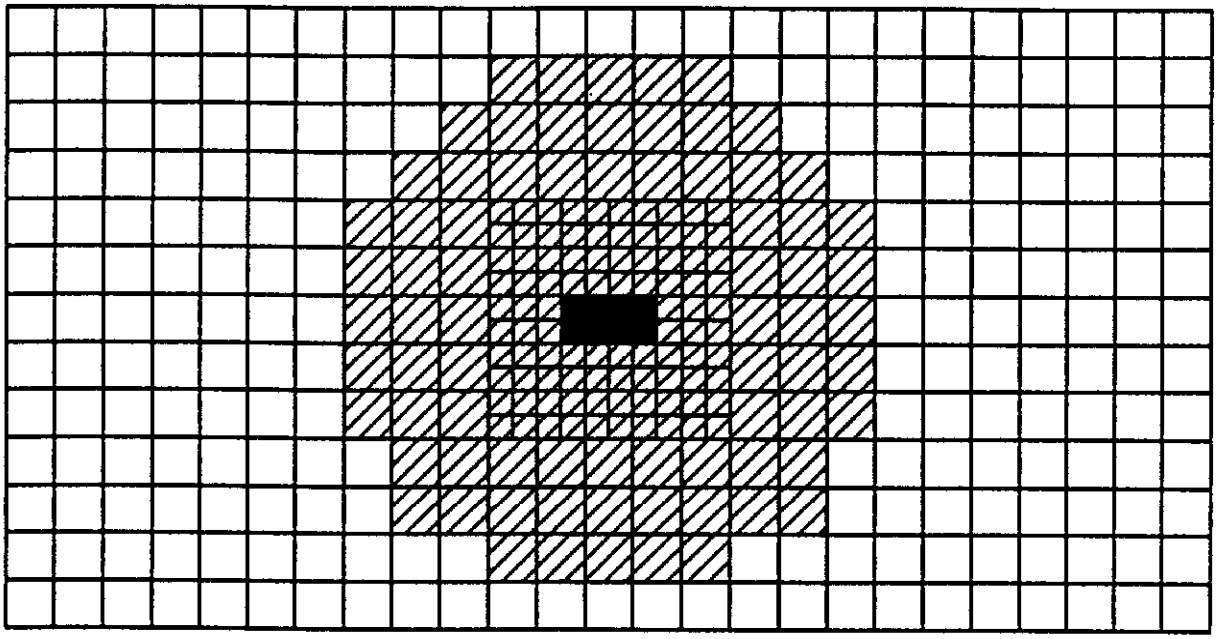

Figure 2. Beam view of the Main Array (SCG1-C scintillating glass is cross-hatched)

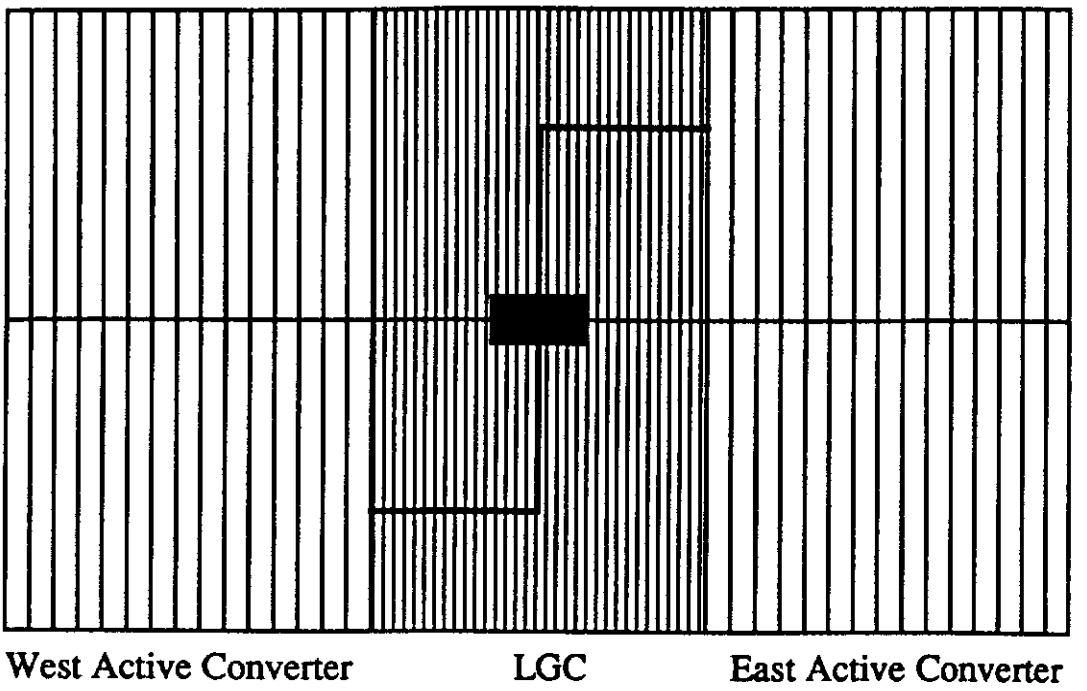

Figure 3. Beam view of the Experiment 705 calorimeter showing West and East Active Converter (AC) and Lead Glass Calorimeter (LGC)

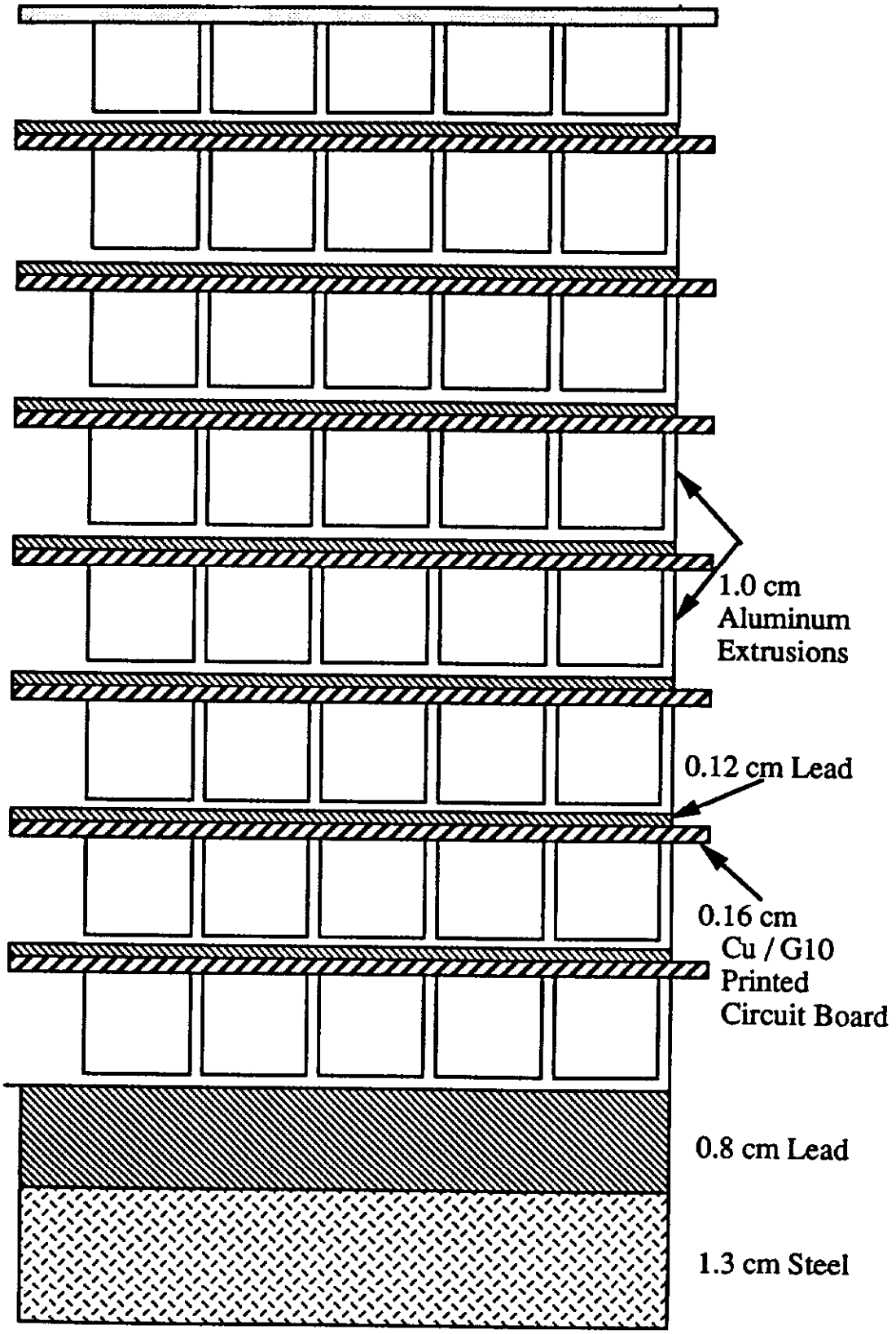

Figure 4. Cross section of the Lead Gas Calorimeter (LGC)

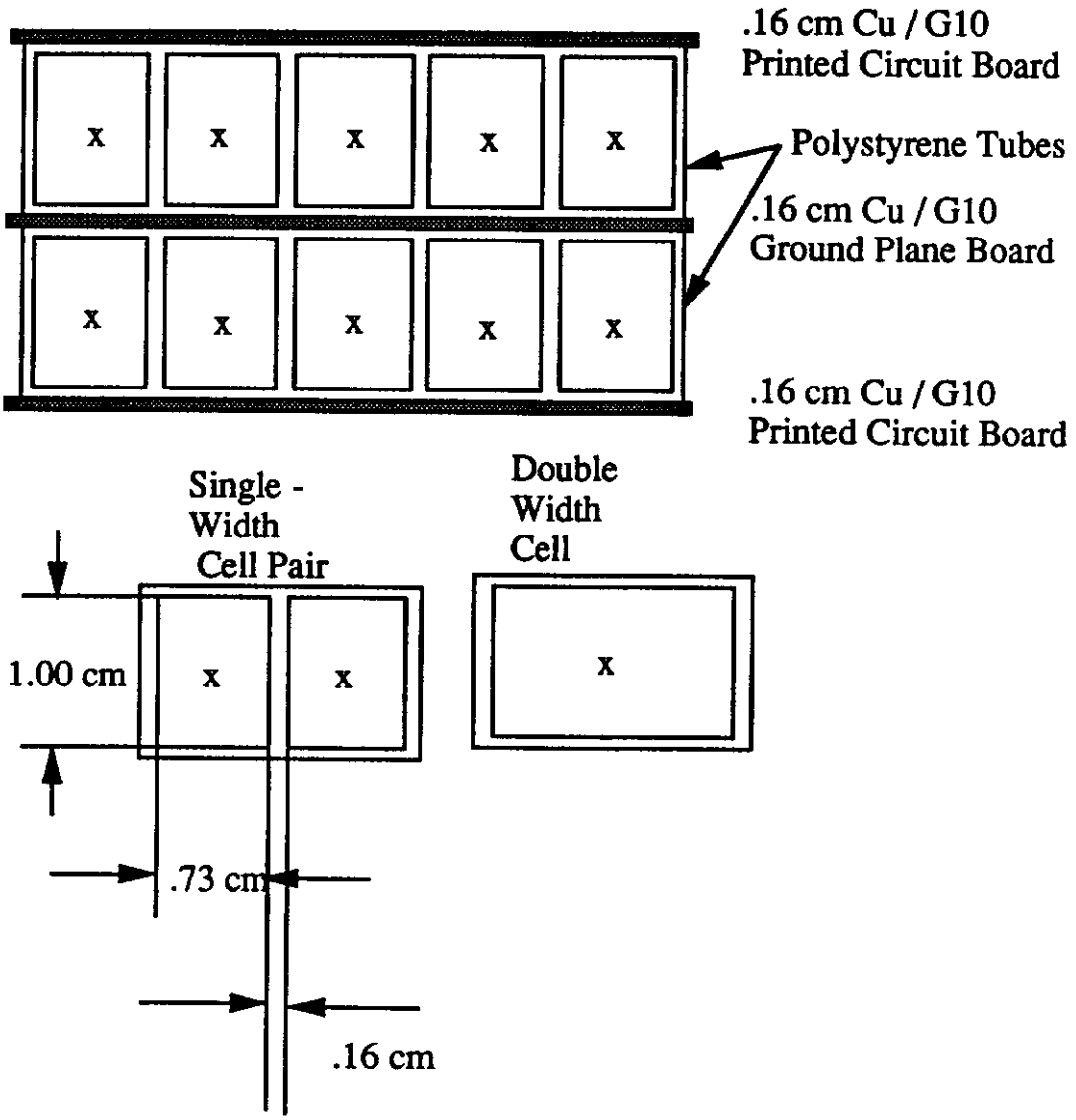

Figure 5. Cross section of the Gas Tube Hodoscope (GTH)

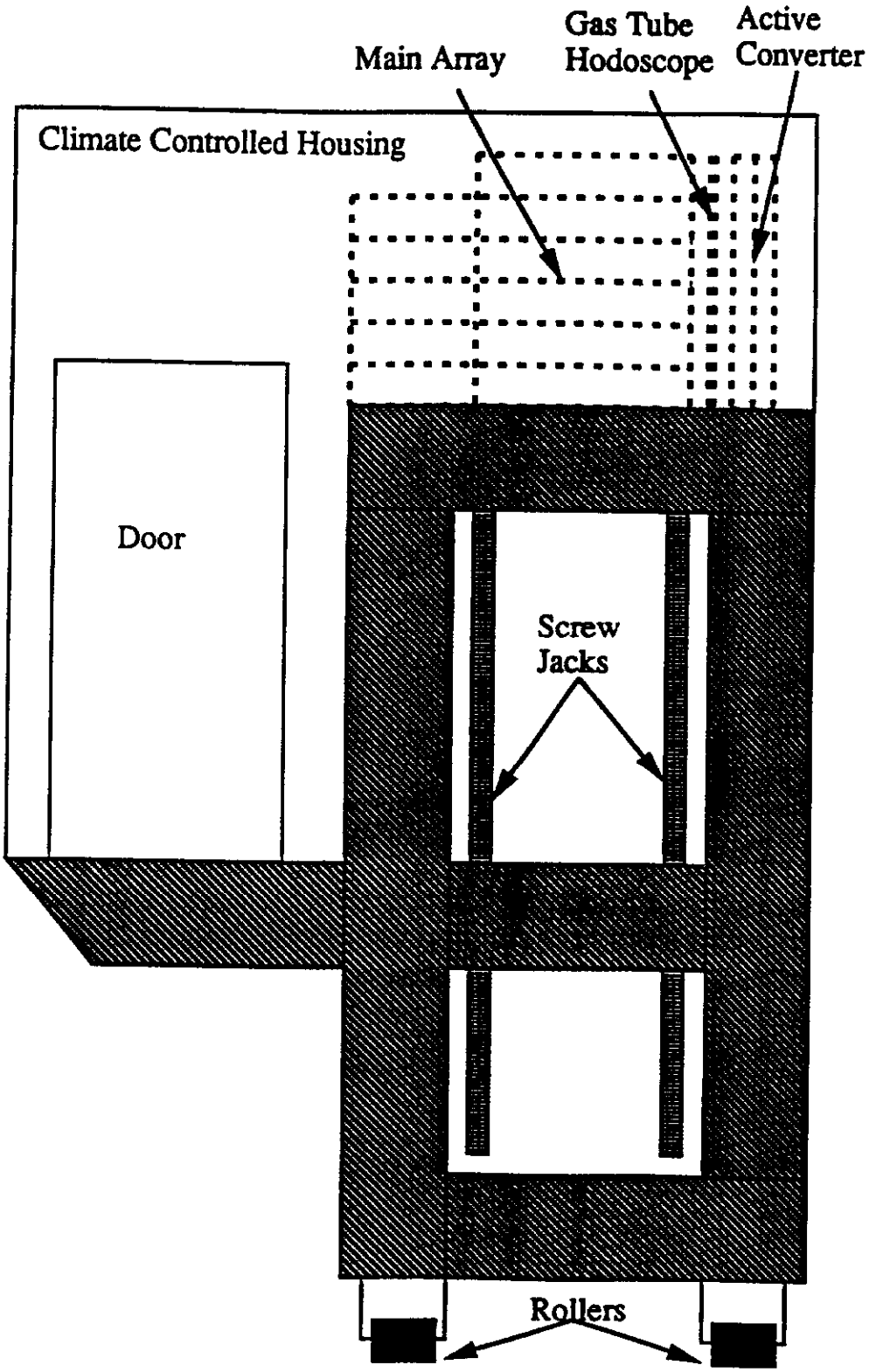

Figure 6. Schematic view of the Experiment 705 calorimeter housing, showing movable table (not to scale)

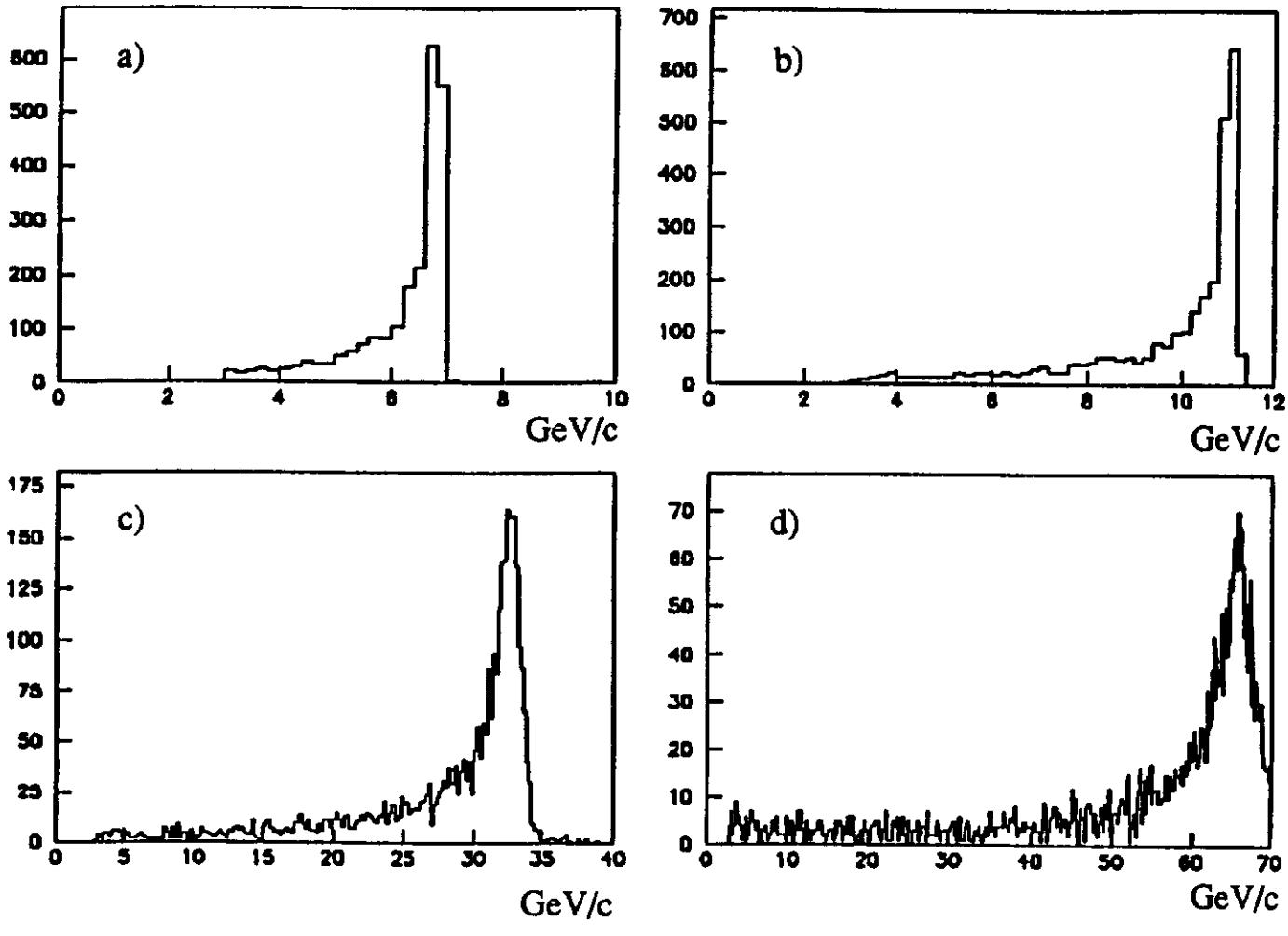

Figure 7. Momentum distributions calibration beams: a) 6 GeV/c, b) 10 GeV/c, c) 30 GeV/c, d) 60 GeV/c

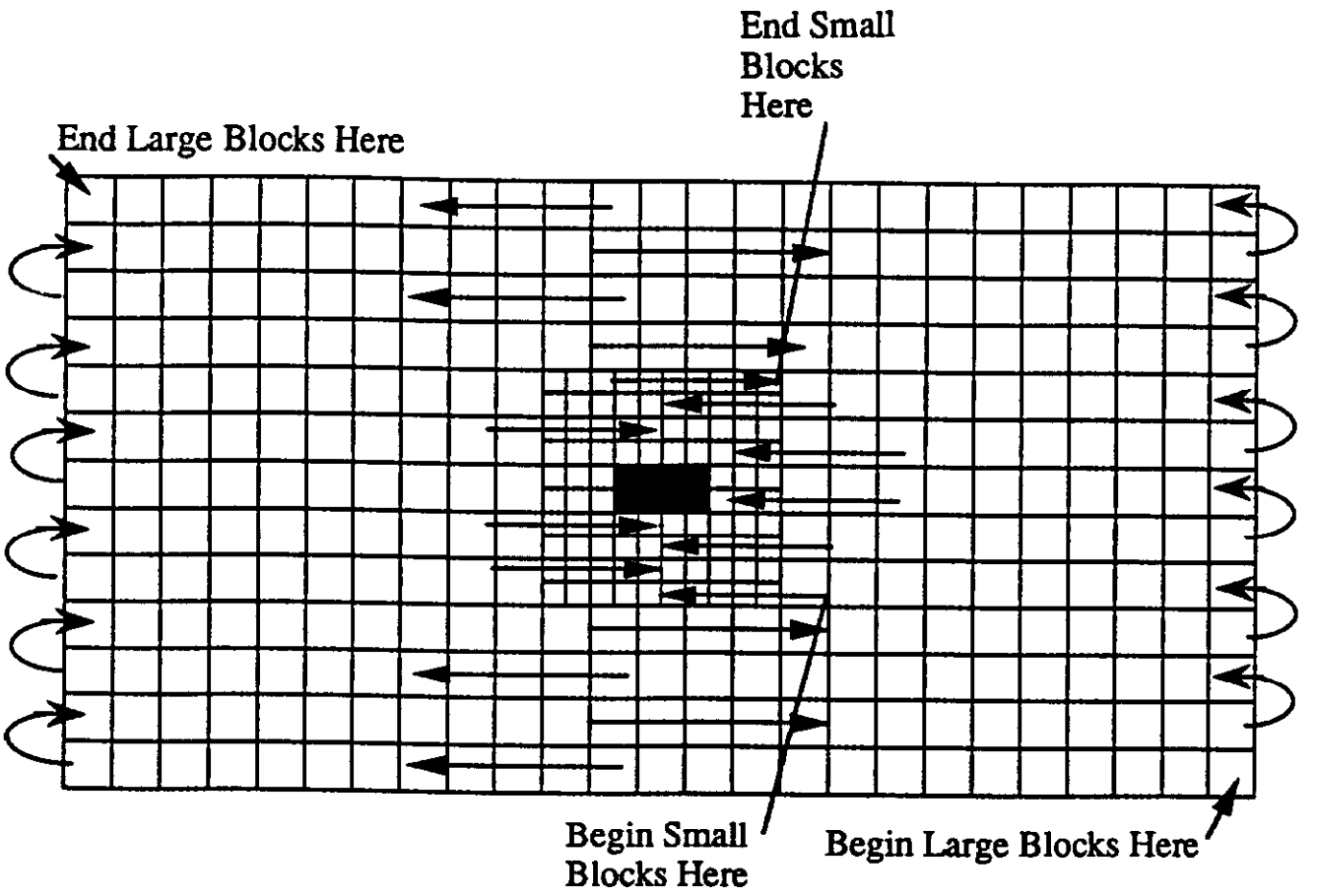

Figure 8. The Main Array glass block calibration sequence

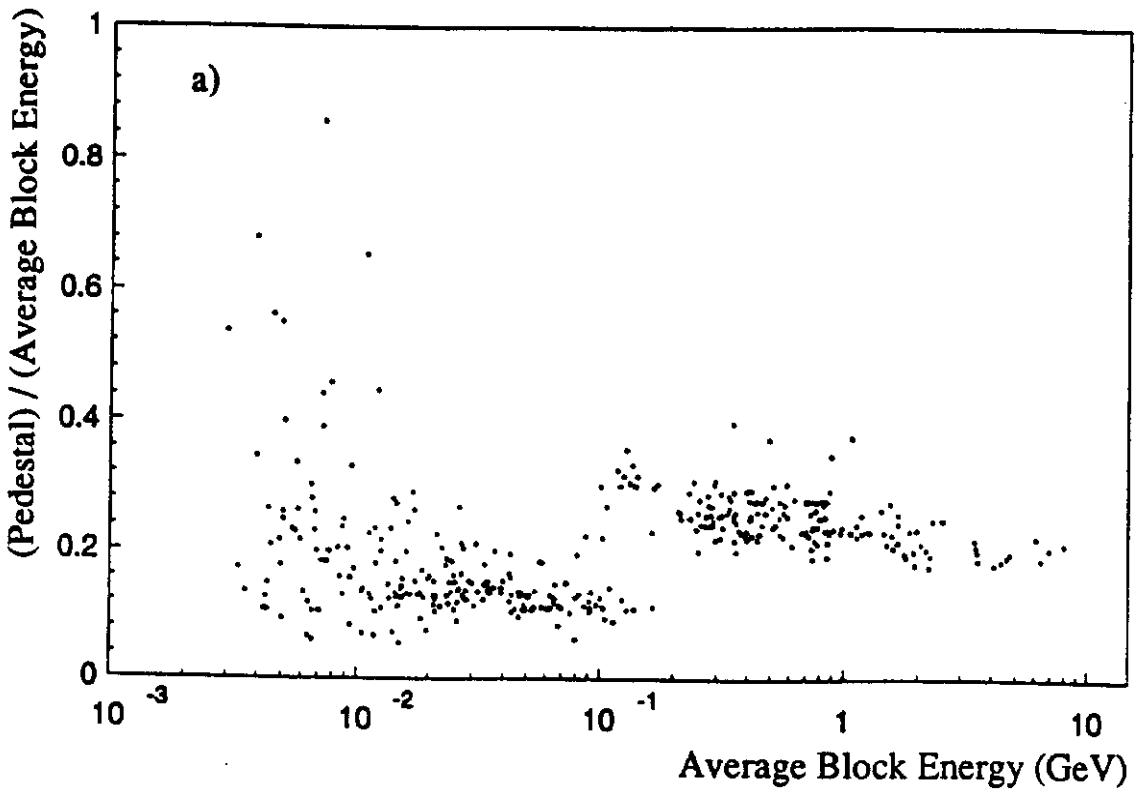

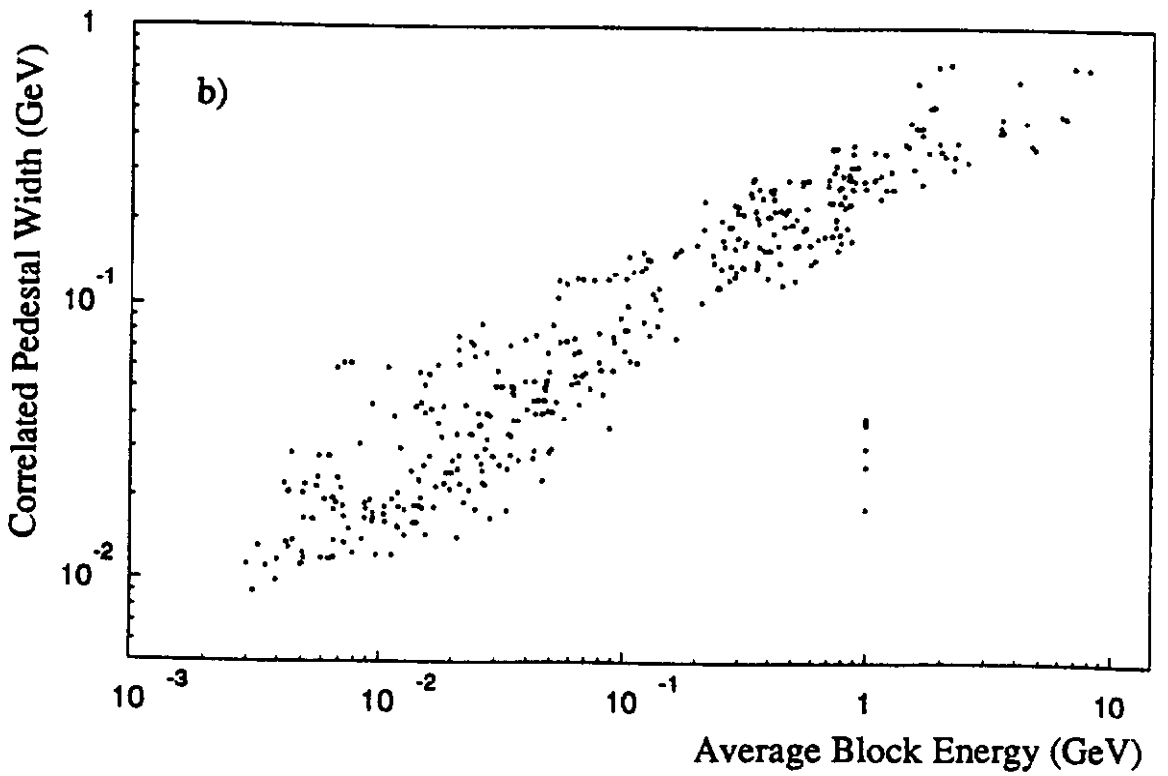

Figure 9. Rate-dependent pedestal effects. As a function of the average energy deposited in a block (inferred from "minimum bias" triggers are shown a) the ratio of the average shift in pedestal to the mean deposited energy, and b) the rms of the pedestal in GeV.

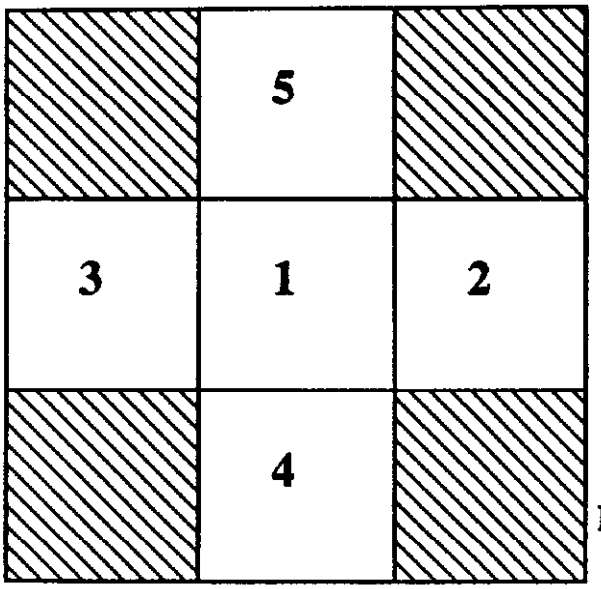

$$p1 = \frac{E1}{E1 + E2 + E3}$$

$$p2 = \frac{E2}{E1 + E2 + E3}$$

$$p3 = \frac{E3}{E1 + E2 + E3}$$

$$p4 = \frac{E4}{E3 + E4 + E5}$$

$$p5 = \frac{E5}{E3 + E4 + E5}$$

$$r_{ij} = \frac{E_i - E_j}{E_i + E_j} \qquad i \neq j$$

i,j = 1,3
1,2
2,3
1,4
1,5
4,5

Figure 10. Block numbering scheme and ratios used in the EGS4 generation of shower patterns for use in the shower position and energy reconstruction algorithms

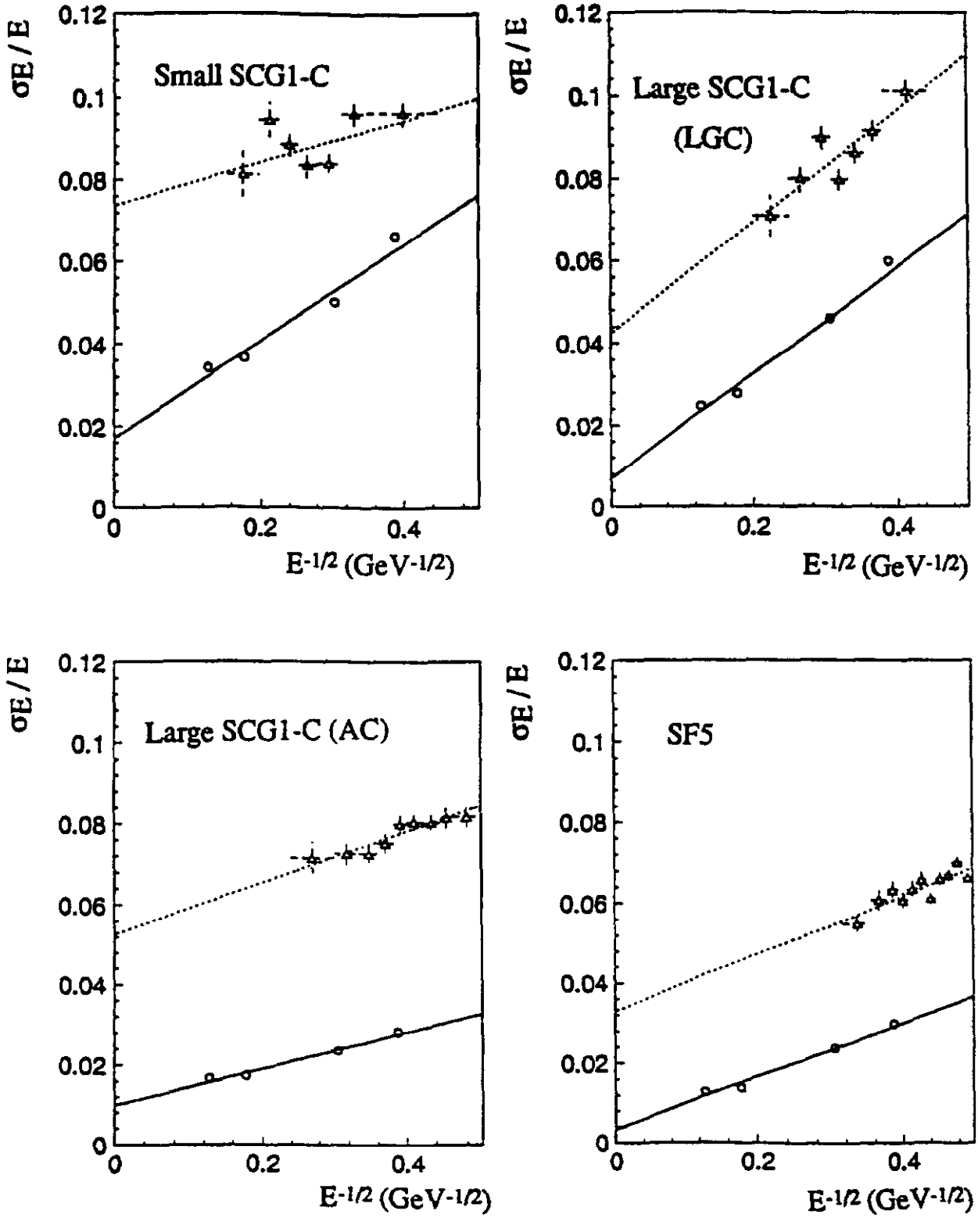

Figure 11. Fractional energy resolution σ(E)/E in various detector regions from calibration data (open circles) and electron/positron pairs in ordinary data (open triangles)

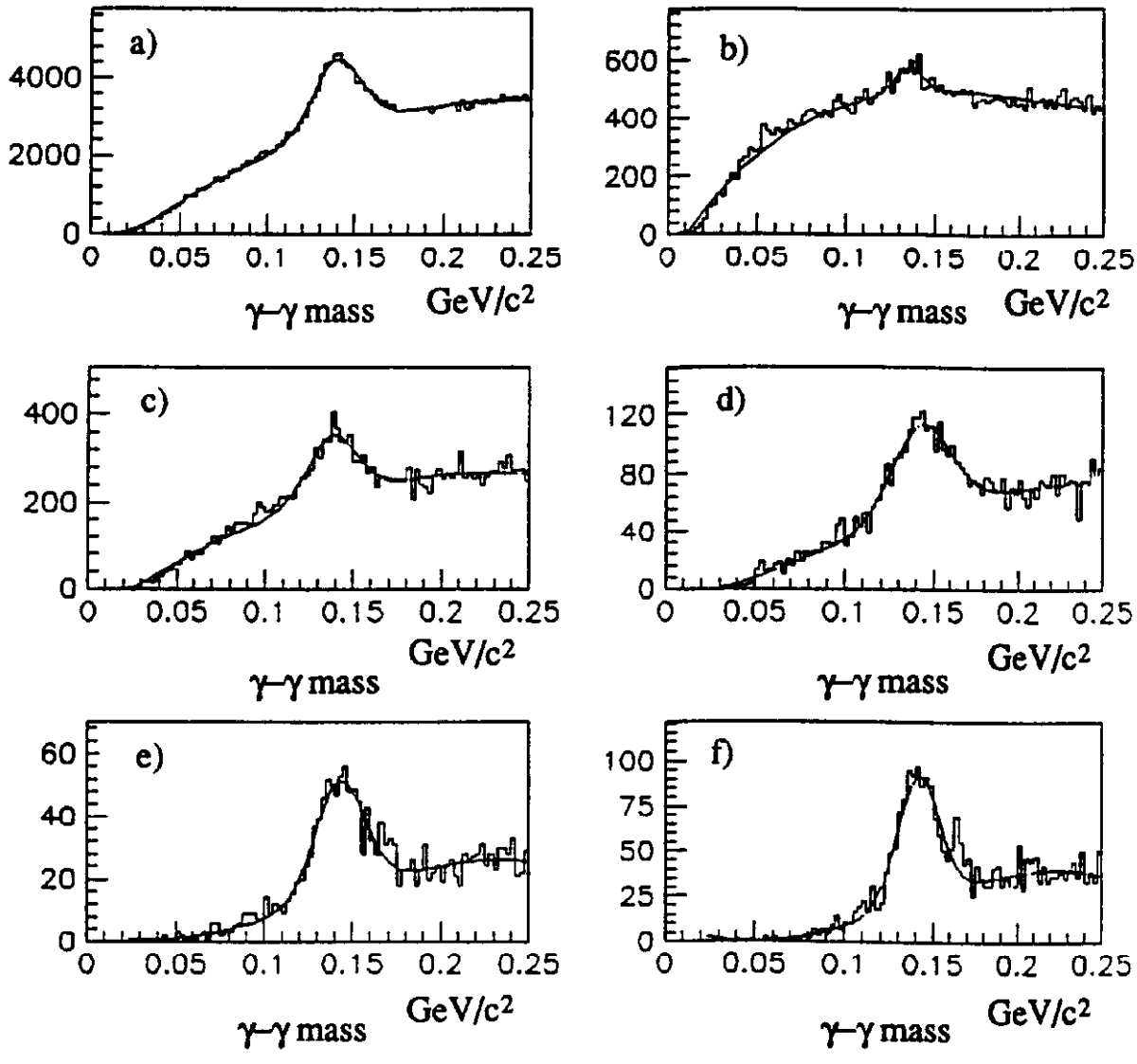

Figure 12. Photon pair invariant mass in the π^0 mass region for various photon energy ranges: a) All energies, b) 1. $\leq E_\gamma$ 3. GeV, c) 3. $\leq E_\gamma$ 5. GeV, d) 5. $\leq E_\gamma$ 7. GeV, e) 7. $\leq E_\gamma$ 9. GeV, and f) 9. $\leq E_\gamma$ 15. GeV. Bin width is 2 MeV/c^2.

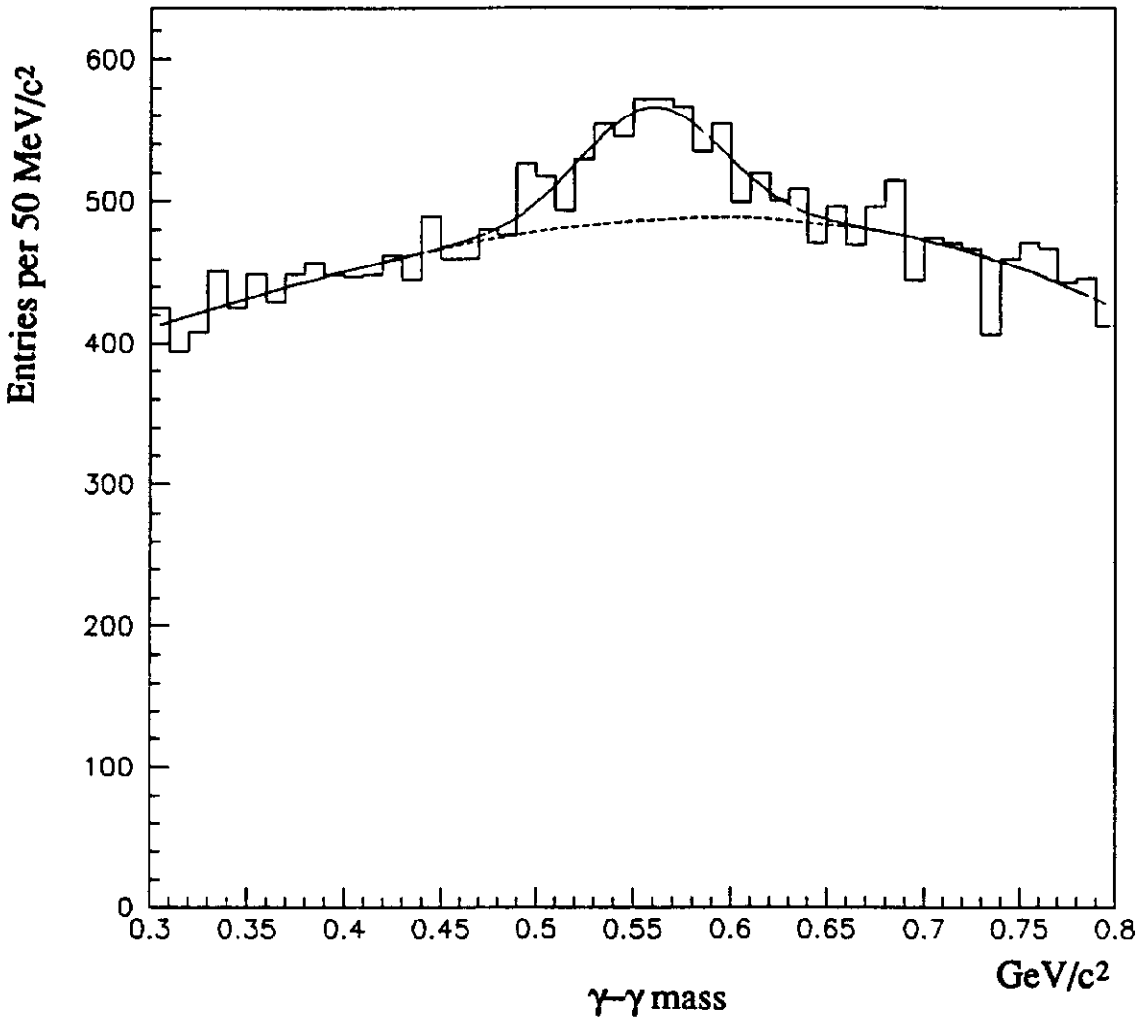

Figure 13. Photon pair invariant mass in the η^0 mass region

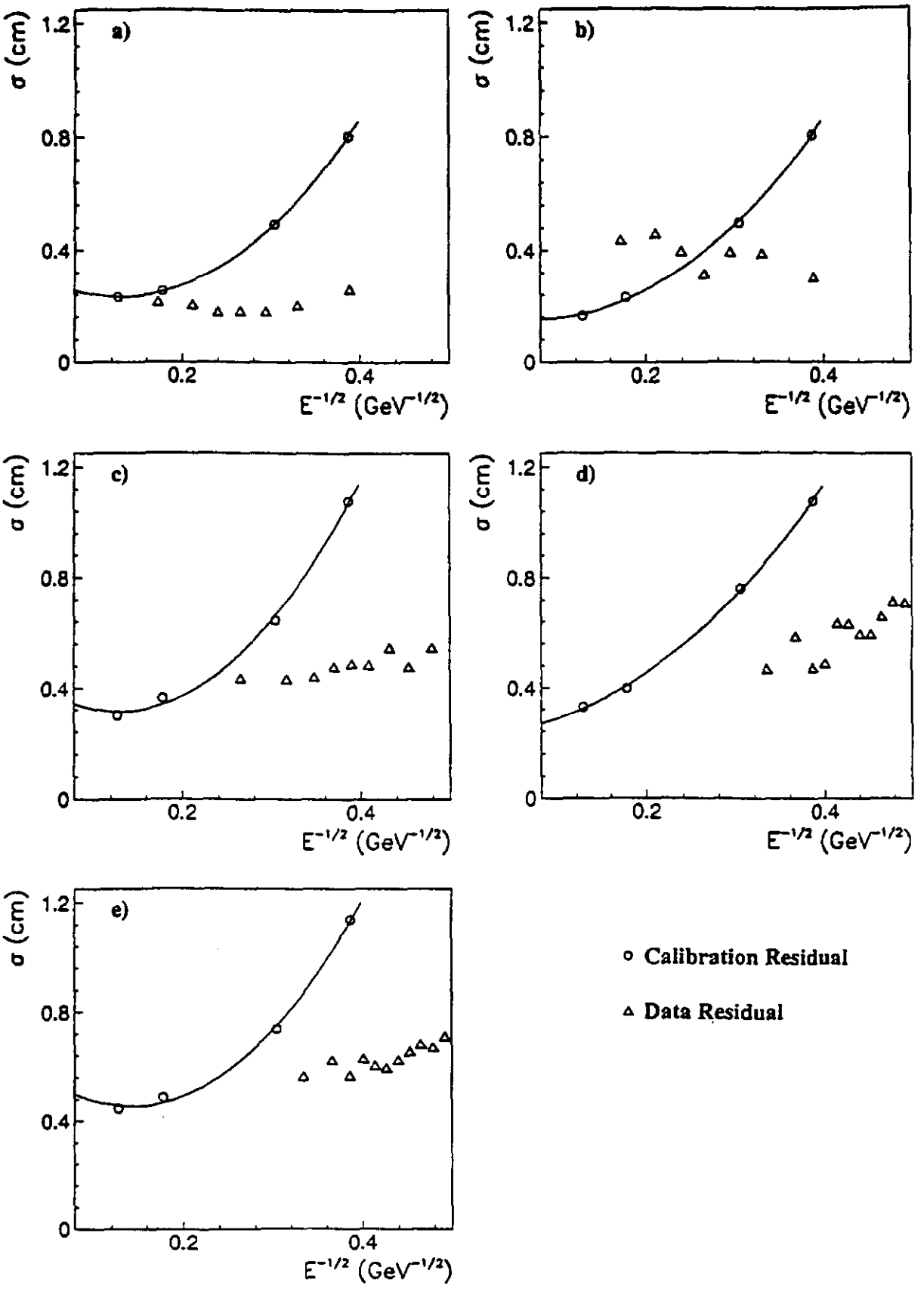

Figure 14. Position resolutions in various regions for calibration data (open circles) and electron/positron pairs from ordinary data (open triangles). The regions shown are (a) LGC, horizontal view; (b) LGC, vertical view; (c) GTH, single-tube width horizontal view; (d) GTH, vertical view; (e) GTH, double tube width horizontal view

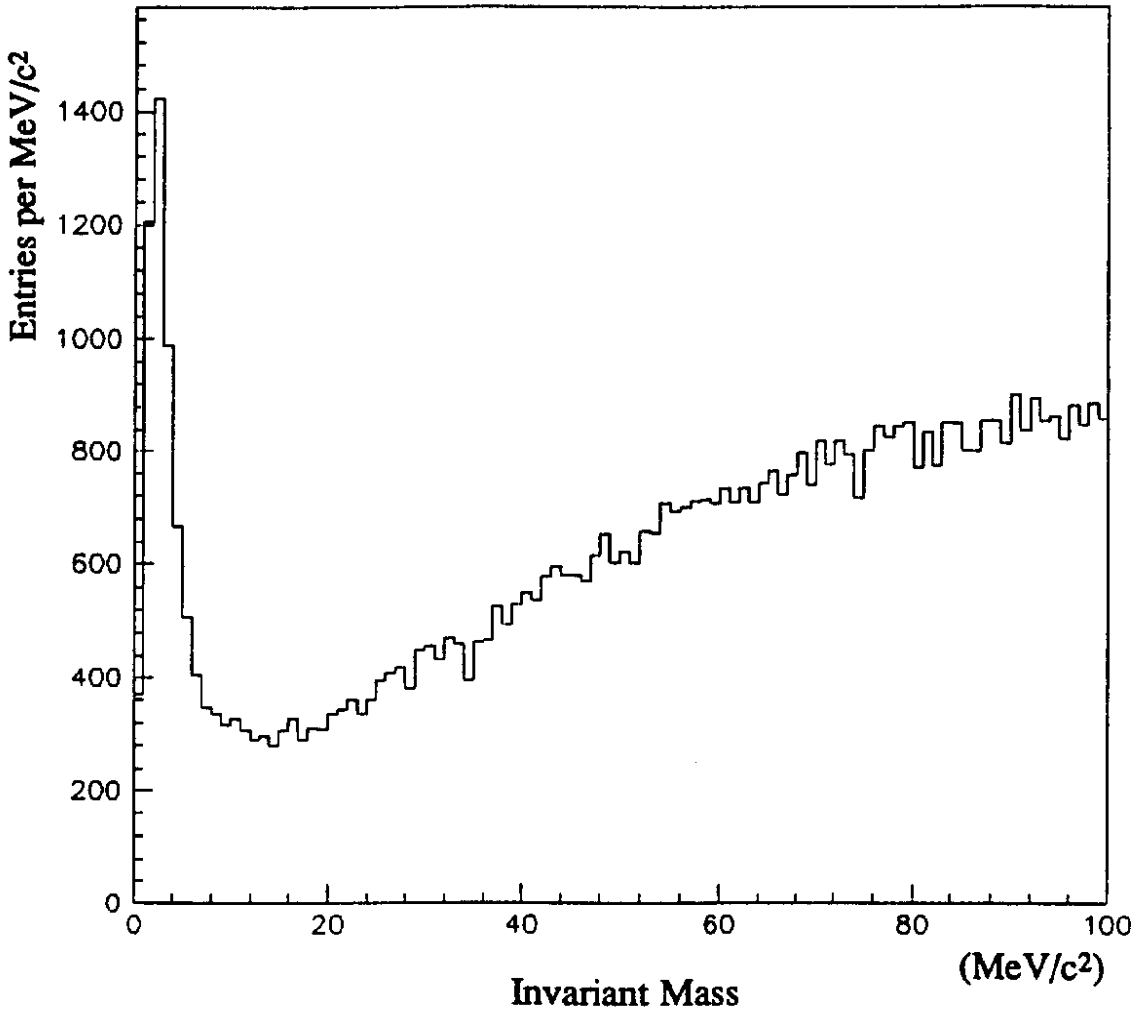

Figure 15. Invariant mass for electron/positron track pairs

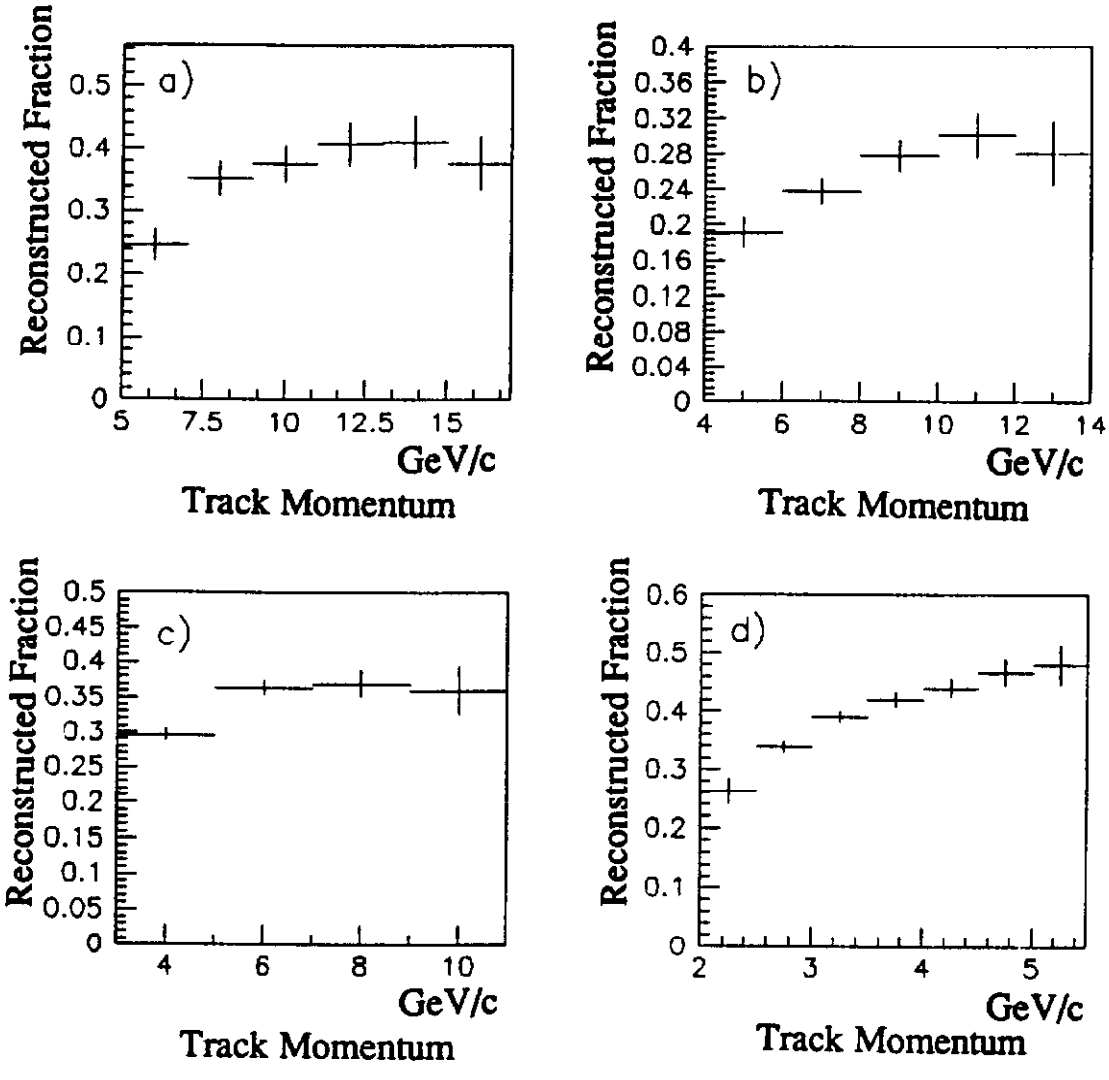

Figure 16. Reconstructed fraction of "partner" tracks (uncorrected reconstruction efficiency) as a function of partner track momentum for (a) small SCG1-C blocks, (b) large SCG1-C blocks with LGC, (c) large SCG1-C blocks with AC and GTH, and (d) SF5 blocks